



AFAPL-TR-78-96

AD AO

# 91999 HIGH EFFICIENCY GaAs SOLAR CELL FINAL REPORT

**Hughes Aircraft Company** Space and Communications Group P.O. Box 92426 Los Angeles, California 90009

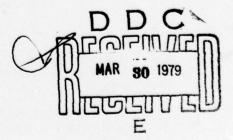
**JANUARY 1979** 

**TECHNICAL REPORT AFAPL-TR-78-96** 

Final Report for Period Covering August 1976 - July 1978

Approved for Public Release, Distribution Unlimited

AIR FORCE AERO PROPULSION LABORATORY AIR FORCE WRIGHT AERONAUTICAL LABORATORIES AIR FORCE SYSTEMS COMMAND WRIGHT-PATTERSON AIR FORCE BASE, OHIO 45433



**HUGHES REF NO. D7870** 

#### NOTICE

When Government drawings, specifications, or other data are used for any purpose other than in connection with a definitely related Government procurement operation, the United States Government thereby incurs no responsibility nor any obligation whatsoever; and the fact that the government may have formulated, furnished, or in any way supplied the said drawings, specifications, or other data, is not to be regarded by implication or otherwise as in any manner licensing the holder or any other person or corporation, or conveying any rights or permission to manufacture, use, or sell any patented invention that may in any way be related thereto.

This report has been reviewed by the Information Office (OI) and is releasable to the National Technical Information Service (NTIS). At NTIS, it will be available to the general public, including foreign nations.

This technical report has been reviewed and is approved for publication.

Carl Stuerpe

Joseph Wise

FOR THE COMMANDER

JAMES D. REAMS

Chief, Aerospace Power Division

"If your address has changed, if you wish to be removed from our mailing list, or if the addressee is no longer employed by your organization please notify AFAPL/POE, W-PAFB, OH 45433 to help us maintain a current mailing list."

Copies of this report should not be returned unless return is required by security considerations, contractual obligations, or notice on a specific document.

AIR FORCE/56780/5 March 1979 - 150

#### UNCLASSIFIED

SECURITY CLASSIFICATION OF THIS PAGE (When Date Entered) READ INSTRUCTIONS BEFORE COMPLETING FORM REPORT DOCUMENTATION PAGE 2. GOVT ACCESSION NO. 3. RECIPIENT'S CATALOG NUMBER AFAPL TR-78-96 HIGH EFFICIENCY GaAs SOLAR CELL Aug 1076 - July 1078 DEVELOPMENT. AUTHOR(+) S. Kamath, G. Wolff F33615-76-C-2121 PROGRAM ELEMENT. PROJECT, TAK AREA & WORK UNIT NUMBERS PE 62203F, Project 3145 PERFORMING ORGANIZATION NAME AND ADDRESS Hughes Aircraft Company Space and Communications Group' Task 314519 Work Unit P.O. Box 92919, Los Angeles, CA 90009 31451961 11. CONTROLLING OFFICE NAME AND ADDRESS Air Force Aero Propulsion Laboratory/POE-2 January 1979 Air Force Wright Aeronautical Laboratories/AFSC NUMBER OF PAGES Wright-Patterson Air Force Base, Ohio 45433

14 MONITORING AGENCY NAME & ADDRESS(If different from Controlling Office) SECURITY CLASS. (of this Unclassified 15a. DECLASSIFICATION DOWNGRADING 16. DISTRIBUTION STATEMENT (of this Report) Approved for public release, distribution unlimited. 17. DISTRIBUTION STATEMENT (of the abstract entered in Block 20, If different from Report) 18. SUPPLEMENTARY NOTES 19. KEY WORDS (Continue on reverse side if necessary and identify by block number) GaAs Solar Cells, Space Power, Solar Energy Conversion ABSTRACT (Continue on reverse side if necessary and identify by block number) The major goals of the High Efficiency Gallium Arsenide (GaAs) Solar Cell program have been met. An AMO efficiency of 17.5 percent was achieved. During the second phase of the program, we optimized the cell structure to improve radiation resistance of the cell without loss of efficiency, thus improving the suitability of the cell for space missions.

391903

18

SECURITY CLASSIFICATION OF THIS PAGE (When Date Entered)

A theoretical model for the radiation resistance characteristics of the GaAs cell was developed and confirmed by experimental data. Based on this, the junction depth was reduced to less than 0.5  $\mu m$  without sacrificing cell efficiency. Radiation annealing at or below 200°C suggests that an end of life efficiency close to that at the beginning of life may be achievable for properly designed cells in space missions.

The Hughes infinite melt epitaxial growth system has demonstrated its capability for making reproducible large area GaAs solar cells. Over 100 4 cm<sup>2</sup> cells fabricated according to our baseline design and using the infinite melt technique were delivered to the Air Force and to Hughes El Segundo for tests. Various fabrication steps such as contacting and AR coating were perfected during the course of the program. Measurements of cell characteristics have been correlated with the theoretical model and the results used to suggest future directions for research to improve the cell performance.

Favorable temperature and humidity test results reported here suggest that GaAs solar cells will be able to pass future rigorous space qualification testing. Cell reliability and solar array packaging remain to be demonstrated. A GaAs solar cell pilot production line is also necessary to demonstrate production environment fabrication and performance.

NTIS DDC UNANNOUNC	Buff S	Section ection	D
UNANNOUNG	turne.		
	ED		
JUSTIFICATI	ON		
	M/AVAC ABO	ITY COME	S
Dist. AV.	Ali	31 1	21.1

#### FOREWORD

This report was prepared by the Hughes Aircraft Company Space and Communications Group, El Segundo, California, under Contract F33615-76-C-2121. The work was administered under the direction of Lt. Stuerke, POE-2, Air Force Aero Propulsion Laboratory, under Program Element 62203F, Project 3145, Task 314519, "High Efficiency GaAs Solar Cell Development."

The period covered extends from 1 August 1976 through 1 July 1978. Contributors include G. Wolff and G. Vendura of the Hughes Aircraft Company Space and Communications Group and S. Kamath, R. Knechtli, R. Loo, and J. Ewan of the Hughes Aircraft Company Malibu Research Laboratories. This report was submitted by the authors in January 1979.

# TABLE OF CONTENTS

		Page
1.	INTRODUCTION	1
II.	THEORETICAL MODEL  1. Short Circuit Current Density  2. Open Circuit Voltage  3. Fill Factor and Power Conversion Efficiency	3 5 15 17
III.	GaAs SOLAR CELL BASELINE DESIGN	23
IV.	EXPERIMENTAL CELL FABRICATION AND RESULTS  1. Cell Fabrication  2. Results  3. Conclusions	25 25 29 45
V.	SOLAR CELL CHARACTERIZATION AND PERFORMANCE  1. Carrier Concentration in Layers  2. Diffusion Length Measurements  3. Junction Depth Measurements  4. Junction Depth Measurements versus Growth Parameters  5. Dark I-V Characteristics  6. Electroluminescence Experiment  7. (AIGa)AS - GaAs Solar Cell Performance	47 47 47 49 51 54 57
VI.	RADIATION RESISTANCE STUDIES 1. Introduction 2. Study Summary	67 67 67
VII.	THERMAL CYCLING, HUMIDITY, AND TAPE PEEL TESTS  1. Thermal Cycling Tests  2. Humidity Tests  3. Tape Peel Tests	77 77 81 81
VIII.	WELDING STUDIES  1. Requirement  2. Cell Characteristics  3. Tab Characteristics  4. Welding Apparatus  5. Bonding Procedure  6. Tab Pull Tests  7. Study Results	83 83 83 85 85 86 87 88
IX.	CONCLUSIONS	93
	REFERENCES	95

# LIST OF ILLUSTRATIONS

		Page
1	Band Structure for GaAs Solar Cell	4
2	Energy Band Diagram for (AlGa)As-GaAs Solar Cell	6
3	(AlGa)As-GaAs Solar Cell Structure	10
4	Short Circuit Current Density versus Electron Diffusion	
	Length in Positive GaAs Layer	12
5	Short Circuit Current Density versus Hole Diffusion Length	13
6	Short Circuit Current Density versus Junction Depth	14
7	Short Circuit Current Density versus Window Layer	
	Thickness	14
8	Open Circuit Voltage versus Base Doping Density	17
9	Power Conversion Efficiency (η) versus Base Diffusion	
	Length (Lp)	20
10	AMO Current versus Voltage of (AlGa) As-GaAs Solar Cell	20
11	GaAs Solar Cell Baseline Design	24
12	Infinite Melt Liquid Phase Epitaxial Growth of GaAs	26
13	2 x 2 cm GaAs Solar Cell with Front Grid Pattern	28
14	GaAs Solar Cell Fabrication and Test	28
15	Typical Photo I-V Characteristics for Cells in Table 7	34
16 1 <b>7</b>	425°C Annealing Temperature Effects (Cell 1817)	40
18	450°C Annealing Temperature Effects (Cell 1817) Dark I-V Characteristics for Cleaved and Divided Areas	41
10	of Cell 1817	42
19	Cell 1822 Photo I-V Characteristics	42
20	EBIC Method of Minority Carrier Diffusion Length	43
	Measurement Using SEM Technique	48
21	SEM Minority Carrier Diffusion Length Measurements	40
	GaAs-GaAs-(AlGa)As Solar Cell	48
22	Junction Depth Determination	50
23	SEM Photos of (AlGa)As-GaAs Solar Cell 283	
	(Magnification 10200X)	50
24	SIMS Measurements on (AlGa) As-GaAs Solar Cell	52
25	Junction Depth (x;) versus Growth Time	54
26	Theoretical Dark I-V Curves for GaAs Solar Cells	56
27	(AlGa)As-GaAs Dark I-V Characteristics	58
28	EBIC Photo of Cross Section of (AlGa)As-GaAs Mesa	
	Structure in Brightness Contrast Mode	59
29	Scanning Electron Micrograph Obtained in EBIC Mode of	
	Same Sample Shown in Figure 28	59
30	Injection IR Luminescence Defect Analysis	
	(AlGa)As-GaAs Solar Cell	60
31	Emission Spots Originating from Defects - Electrolumi-	
	nescence Experiment on(GaAs)As-GaAs Solar Cell 433	/.
	Using Infrared Microscope	61

# LIST OF ILLUSTRATIONS (concluded)

		Page
32	Emission Spots Originating from Defects - Reverse Biased	
	Image of (GaAl) As-GaAs Solar Cell in Optical Microscope	62
33	(GaAs)As-GaAs Solar Cell Photo I-V	62
34	Spectral Response, Cell 526	64
35	Short Circuit Current Density versus (AlGa)As Layer	
	Thickness	65
36	Voc versus Base Doping Density	65
37	Maximum Power as Function of 1 MeV Electron Fluence	68
38	(AlGa)As-GaAs Solar Cell Spectral Response Before and	
	After 1 MeV Electron Irradiation	68
39	Short Circuit Current Density versus 1 MeV Electron	
,	Radiation Fluence	68
40	Predicted (AlGa)As-GaAs Solar Cell Short Circuit Current	
	Density versus 1 MeV Electron Radiation Fluence	70
41	Short Circuit Current versus Electron Fluence Level	
_	(1 MeV)	70
42	Maximum Output Power versus 1 MeV Electron Fluence	72
43	(AlGa)As-GaAs Solar Cell Spectral Response versus	
	1 MeV Electron Radiation	72
44	Shallow Junction Cell Spectral Response for Several	
	Electron Energies	74
45	Dark I-V Characteristics Before and After Electron	
	Irradiation	74
46	Unannealed Fraction versus Annealing Time	74
47	(AlGa)As-GaAs Solar Cell Spectral Response	75
48	Dark I-V Characteristics Before and After Thermal	
	Annealing	76
49	Photo I-V Characteristics Before and After Thermal	
	Cycling Test	78
50	Photo I-V Characteristics Before and After Humidity	
	Test	80
51	Silver Foil Pattern Consisting of Six Tabs	84
52	Top View Schematic of Ultrasonic Wheel-Welder and	
	Supporting Equipment	84

# LIST OF TABLES

		Page
1	References for $\alpha(\lambda)$ , $k(\lambda)$ , and $n(\lambda)$ for Cell Materials	10
2	FF and η for Several Different Values of Series Resistance	19
3	Experimental Data for $(Al_x Ga_{1-x})$ - GaAs Solar Cell No. 373	21
4	HRL GaAs Solar Cell Characteristics: January 1976	30
5	HRL GaAs Solar Cell Characteristics: June 1976	30
6	HRL GaAs Solar Cell Characteristics: January 1977	30
7	(AlGa) As-GaAs Solar Cell Characteristics (AM0)	35
8	Role of Oxygen in (AlGa) As Layers: Electrical	
	Characteristics	36
9	Effect of Annealing on Cell Performance	39
10	GaAs Cells with Very Shallow Junctions	44
11	Hall Effect Measurement Results	47
12	Diffusion Lengths Measured in Each Layer of (AlGa)	
	As-GaAs Solar Cell	49
13	Techniques Used for Junction Depth Measurements	51
14	Junction Depth Measurements versus Growth Parameters	53
15	Junction Depth Measurements versus Growth Time for	
	Radiation Resistant Cells	54
16	HRL GaAs Solar Cell Characteristics (January 1977)	63
17	Electron Irradiation Experiment Test Matrix	69
18	Electrical Parameters Before and After Humidity Test	81
19	Tab Pull Results for Silicon Solar Cell S101	89
20	Tab Pull Results for GaAs Solar Cell 2M928	90
21	Tab Pull Results for GaAs Solar Cell 2M1098	91
22	Tab Pull Results for GaAs Solar Cell 1E981	91
23	Tab Pull Results for GaAs Cell 1E1021A	92

# GLOSSARY

# ABBREVIATIONS AND ACRONYMS

air mass zero
electron beam induced current
fill factor
High Efficiency Solar Panel program
Hughes Research Laboratories (Malibu, CA)
independent research and development
Jet Propulsion Laboratory (Pasadena, CA)
liquid phase epitaxy
parts per million
Hughes Aircraft Company Space and Communications Group
scanning electron microscope
secondary ion mass spectroscopy

# SYMBOLS

A	area of cell
a(X)	absorption coefficient
D	(AlGa)As layer thickness
$D_a/D_p/D_n$	diffusion constants
η	power conversion efficiency
$F(\lambda)$	number of incident protons/cm <sup>2</sup> /sec
I	diode leakage current
I sc	short circuit current density
I-V	current-voltage

wavelength λ Lp hole diffusion length effect of space charge region recombination; junction perfection factor n base doping density  $N_D$ index of refraction  $n(\lambda)$ series resistance  $R_s$ Tg growth temperature t g V oc growth time open circuit voltage junction depletion width junction depth

#### SECTION I

### INTRODUCTION

This report covers the work performed on the High Efficiency GaAs Solar Cell Development program (August 1976 through 1 July 1978). The objective of this program was to develop gallium arsenide solar cells having 18 to 20 percent efficiency at 25°C under single sun intensity air mass zero (AMO) illumination. The plan included fabrication of the epitaxial structure, (AlGa) As-GaAs, using the Hughes infinite melt technique, and a demonstration that high efficiency solar cells based on this structure can be reproducibly fabricated with areas of 4 cm² using processing methods suitable for large scale production.

We essentially achieved our objectives with the fabrication of 17.5 percent efficient 2 x 2 cm solar cells possessing radiation resistance characteristics superior to those of existing silicon solar cells. Furthermore, we developed a theoretical model for (AlGa) As-GaAs cells that can be used for future improvement of space-qualified cells. The fabrication processes and techniques used during the program can be directly scaled up to production of mass quantities of GaAs solar cells.

The goal of approximately 18 percent efficiency was achieved during the program; however, cells with these efficiencies possessed less than the desired radiation resistance. We found that making the junction shallower provided the desired radiation resistance, at the expense of some efficiency. The last part of the program, therefore, was concerned with increasing the efficiency once again, while keeping the radiation resistance at the desired level. An efficiency of 17.5 percent was achieved before the program was terminated because of funding constraints.

Section II of this report describes the theoretical model for the GaAs solar cell, giving the reasons for choosing the p-on-n structure and providing calculations for short circuit current, open circuit voltage, fill factor, and cell efficiency. Section III presents the baseline structure for the (AlGa)As-GaAs solar cell.

Section IV describes the approach used for liquid phase epitaxy, the reasons for its choice, and the experimental results. A good deal of silicon solar cell development technology has been drawn on, minimizing the development cost and time required to achieve the targets of the program.

Section V presents a detailed analysis of the characteristics of the cells produced and a correlation of their performance with the model. The areas in which the correlation needed to be improved are indicated, and the parameters such as junction depth, carrier concentration, etc., which can lead to improved performance of the cells are discussed. One of the most important components is the ohmic contacts to the n and p layers of the cell. We use Au-Zn and Au-Ge-Ni systems for contacting the p and n sides, respectively. Although limited to about 450 to 500°C by their metallurgy, they are simple, well-tried systems that cover the needs of the program. The Ag-Zn, Ag-Sn system and others using refractory metals promise to extend the performance limits of the cells to higher temperatures (600°C).

Section VI discusses the radiation resistance results obtained. Sections VII and VIII deal with interconnect problems and environmental studies on the cell. These need to be expanded to complete the evaluation of the GaAs cell for long life in space systems.

Section IX is a brief summary of the conclusions that can be drawn from the present data.

#### SECTION II

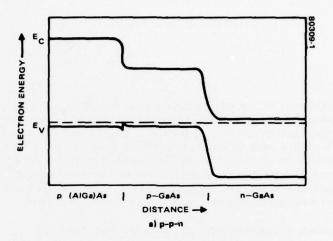
#### THEORETICAL MODEL

The basic structure of the GaAs solar cell is a GaAs p-n junction covered by a window layer of (AlGa)As; the surface is covered by an antireflection coating and provided with ohmic electrical contacts on both sides. The operations of the cell to convert optical solar energy to electrical energy are similar to those of the silicon solar cell. Since the (AlGa)As layer adds a new dimension to the structure that is specific to the GaAs cell, this aspect needs special consideration. The model for the cell was developed from available literature and from our own data.

The p-on-n structure was chosen for two reasons. First, since the diffusion length of electrons in the player is longer than that of holes in comparably n-doped GaAs, the response of the cell is improved by using the p-type layer in the optically absorbing top region. Second, the interfacial barrier is considered to be smaller for the p (AlGa)As - p GaAs (0.1 eV) than for the n (AlGa)As - n GaAs case (0.3 eV) (see Figure 1). Since these barriers act like Schottky barriers in series with the solar cell, they increase the series resistance of the cell and adversely affect the fill factor. We used this basic approach to derive parameters for optimized cell performance during the first phase of the program (Section IV). The final baseline structure is given in Figure 11 (see Section III).

This section provides calculations for the short-circuit current, open circuit voltage, fill factor, and efficiency of the GaAs solar cells. We set up a computer program with these factors to calculate the cell performance as a function of various parameters; the program was updated as better values for these parameters became available, and was used to optimize the cell design.

Comparison of the theoretical model with cell data (Section V) demonstrated the need for a more accurate determination of such parameters as minority carrier lifetimes and optical data in the various layers in the device to obtain an accurate picture of the operation of the cell. We did obtain a more accurate experimental definition of the junction quality factor n (effect of space charge region recombination) and of the contribution of various regions in the cell to the electrical parameters (e.g., series resistance), as noted in succeeding sections of this report.



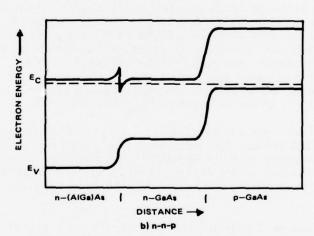


FIGURE 1. BAND STRUCTURE FOR GaAs SOLAR CELL

The computerized model was used to correlate theory with experimentally measured values, and the findings were used to vary growth parameters and tailor the epitaxial layer properties for improved device performance. The success of this approach is demonstrated by the determination and control of the junction depth to minimize radiation damage in the GaAs cell (Section VI).

# 1. SHORT CIRCUIT CURRENT DENSITY (Isc)

This subsection computes the short circuit current density of the (AlGa)As-GaAs solar cell.

When light of wavelength  $\lambda$  is incident on the surface of a semiconductor, the generation rate of electron-hole pairs as a function of distance x from the surface is

$$G(\lambda, x) = \alpha(\lambda) F(\lambda) \exp(-\alpha(\lambda) x) [1 - R(\lambda)]$$

where  $\alpha(\lambda)$  is the absorption coefficient of a material,  $F(\lambda)$  is the number of incident photons per cm<sup>2</sup> per second, and R is the fraction reflected from the surface. To calculate solar cell output one must determine the number of photo-excited minority carriers that reach the p-n junction and are collected. For a low injection level condition the minority carrier continuity equations are

$$D_{p} \frac{d^{2} \Delta p}{dx^{2}} + G_{p} - \frac{\Delta p}{r_{p}} = 0$$

for holes in n-type material. Similarly,

$$D_{n} \frac{d^{2} \Delta n}{dx^{2}} + G_{n} - \frac{\Delta n}{\tau_{n}} = 0$$

for electrons in p-type material, where  $\Delta p$  and  $\Delta n$  are the excess carrier densities,  $D_p$  and  $D_n$  are the diffusion constants, and  $\tau_p$  and  $\tau_n$  are the hole's and electron's minority carrier lifetime, respectively.

The short circuit current produced by the absorption of solar photons of one specific wavelength is the sum of the specific contributions from all layers of the solar cell shown in Figure 2. These contributions are given below.

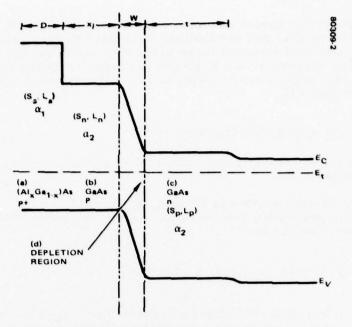


FIGURE 2. ENERGY BAND DIAGRAM FOR (AIGa)As-GaAs SOLAR CELL

# · Collection From the (AlGa)As Window Layer

The minority carrier continuity equation for the photogenerated electrons in this layer is

$$D_{a} \frac{d^{2} \Delta n}{dx^{2}} + \alpha_{1} (1 - R(\lambda)) F e^{-\alpha_{1} x} - \frac{\Delta n}{\tau_{a}} = 0$$
 (1)

where D is the diffusion constant,  $\alpha_1$  is the absorption coefficient, and  $\tau_a$  is the electron lifetime in the p<sup>+</sup> (AlGa)As layer.

The boundary condition at the window surface is determined by surface recombination velocity  $\mathbf{S}_{\mathbf{a}}$ .

$$S_{\mathbf{a}} \Delta \mathbf{n} \Big|_{\mathbf{x}=0} = D_{\mathbf{a}} \frac{\mathrm{d}\Delta \mathbf{n}}{\mathrm{d}\mathbf{x}}$$
 (2)

and at the interface

$$\Delta \mathbf{n} \bigg|_{\mathbf{X}} = \mathbf{D} \tag{3}$$

The short circuit current density contribution from the window layer is

$$I_{D} = q D_{a} \frac{d\Delta n}{dx} \bigg|_{x=D}$$
(4)

After solving for  $\Delta n$  and applying Equation 4, the current density per unit wavelength is given by

$$I_{D} = \frac{qF\alpha_{1}L_{a}(1-R(\lambda))}{(\alpha_{1}^{2}L_{a}^{2}-1)} \left[ \frac{\alpha_{1}L_{a}+S_{a}\frac{T_{a}L_{a}}{L_{a}}\left(1-e^{-\alpha_{1}D}Cosh\frac{D}{L_{a}}\right)-e^{-\alpha_{1}D}sinh\frac{D}{L_{a}}}{Sa\frac{T_{a}}{L_{a}}sinh\frac{D}{L_{a}}+cosh\frac{D}{L_{a}}} - \alpha_{1}L_{a}e^{-\alpha_{1}D} \right]$$

$$-\alpha_{1}L_{a}e^{-\alpha_{1}D}$$
(5)

where  $L_a$  is the electron diffusion length in the (AlGa)As layer. This current density is that of the electrons being injected into the p-GaAs region from the window layer.

# Collection from p-GaAs Region

is

The minority carrier continuity equation for electrons in the p-GaAs

$$D_{n} \frac{d^{2}\Delta n}{dx^{2}} + \alpha_{2}(1 - R(\lambda)) \operatorname{Fe}^{-\alpha_{1}D - \alpha_{2}(x - D)} - \frac{\Delta n}{\tau_{n}} = 0$$
 (6)

where Fe<sup>- $\alpha_1$ D(1 - R( $\lambda$ )) is the attenuated photon flux at wavelength  $\lambda$ , and  $\alpha_2$  is the absorption coefficient in p-GaAs. The boundary condition at the interface on the (AlGa)As window layer side is</sup>

$$D_{n} \frac{d\Delta n}{dx} \bigg|_{x=D} = S_{n} \Delta n - \frac{I_{D}}{q}$$
(7)

and at the junction edge

$$\Delta \mathbf{n} \Big|_{\mathbf{x} = \mathbf{D} + \mathbf{x}_{\mathbf{j}}} = 0 \tag{8}$$

where  $D_n$  is the electron diffusion constant in p-GaAs and  $S_n$  is the surface recombination velocity at the interface between (A1Ga)As and GaAs.

After solving for the electron density, the short circuit current (density per unit wavelength) at the junction edge is

$$I_{p} = \frac{qFe^{-\alpha_{1}D} (1 - R(\lambda)) \alpha_{2} L_{n}}{(\alpha_{2}^{2} L_{n}^{2} - 1)}$$

$$\chi \left[ \frac{\alpha_2 \frac{L_n + S_n \frac{\tau_n}{L_n} \left( 1 - e^{-\alpha_2 x_j} \cosh \frac{x_j}{L_n} \right) - e^{-\alpha_2 x_j} \sinh \frac{x_j}{L_n}}{S_n \frac{\tau_n}{L_n} \sinh \frac{x_j}{L_n} + \cosh \frac{x_j}{L_n}} - \alpha_2 L_n e^{-\alpha_2 x_j} \right]$$

$$+\frac{I_{D}}{S_{n}\frac{\tau_{n}}{L_{n}}\sinh\frac{x_{j}}{L_{n}}+\cosh\frac{x_{j}}{L_{n}}}$$
(9)

where Ln is the electron diffusion length in p-GaAs.

# Collection from Base n-GaAs Region

The minority continuity equation for holes in the base n-GaAs is

$$D_{p} \frac{d^{2} \Delta P}{dx^{2}} + \alpha_{2} (1 - R(\lambda)) F e^{-\alpha_{1} D} e^{-\alpha_{2} (x_{j} + w)} e^{-\alpha_{2} (x - D - x_{j} - w)}$$

$$-\frac{\Delta \mathbf{P}}{r_{\mathbf{p}}} = 0 \tag{10}$$

where  $w = (2\epsilon\epsilon_0 V_a/qN_D)^{1/2}$  is the junction depletion width based on abrupt junction theory (see Junction Depth Measurements in Section V).

At the junction edges the boundary condition is

$$\Delta \mathbf{p} \bigg|_{\mathbf{x} = \mathbf{D} + \mathbf{x}_{j} + \mathbf{w}} = 0 \tag{11a}$$

At the back interface the boundary condition is

$$D_{\mathbf{p}} \frac{d\Delta \mathbf{P}}{d\mathbf{x}} \bigg|_{\mathbf{x} = \mathbf{D} + \mathbf{x}_{\mathbf{j}} + \mathbf{w} + \mathbf{t}} = \mathbf{S} \mathbf{p} \ \Delta \mathbf{p}$$
(11b)

We assume further that t (the cell base thickness) has values large enough so that

$$t \gg 1/\alpha_2$$
 and  $t \gg L_p$  (12)

The short circuit current density per unit wavelength collected from the base is then given by

$$I_{b} = \frac{q F (1 - R(\lambda)) e^{-\alpha_{1}D} \alpha_{2} L_{p}}{(\alpha_{2} L_{p} + 1)} e^{-\alpha_{2}(x_{j} + w)}$$
(13)

where Lp is the hole diffusion length in n-GaAs.

TABLE 1. REFERENCES FOR  $\alpha(\lambda)$ ,  $k(\lambda)$ , AND  $n(\lambda)$  FOR CELL MATERIALS

		References		
Material	Remarks	n(λ)	k(X)	a (X)
MgF2 (blooming layer)		1	2	
Glass	Corning 7940 (fused silica)	3	3	
Ta <sub>2</sub> O <sub>5</sub>	Thickness = 684 Å	4	5	
Adhesive	XR-63-488	6		
GaAs		7.	7*	
Ga <sub>x</sub> A1 <sub>1-x</sub> As	x = 0.97 Eg = 1.439 + 1.042x + 0.468x <sup>2</sup>	8		9*, 10**

\*Both n- and p-type GaAs were assumed to have the same absorption coefficient.

\*\*Data were obtained by using the absorption coefficient of GaP, which is qualitatively similar to the absorption edge of GaAs, and by transposing resulting absorption data as a function of energy onto the direct bandgap energy value E<sub>g</sub> of Ga<sub>X</sub>A1<sub>1-X</sub>As.

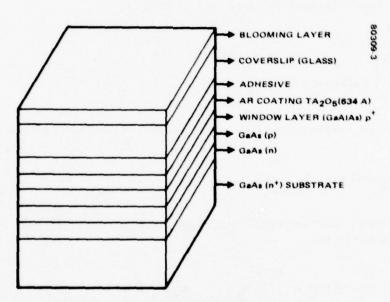


FIGURE 3. (AIGa)As-GaAs SOLAR CELL STRUCTURE

# • Collection From Depletion Region

The current density generated in the depletion region is given by

$$I_{\mathbf{w}} = \mathbf{q} \mathbf{F} (1 - \mathbf{R}(\lambda)) e^{-\alpha_1} \mathbf{D} \begin{pmatrix} -\alpha_2 \mathbf{w} \\ 1 - \mathbf{e} \end{pmatrix} e^{-\alpha_2 \mathbf{x}} \mathbf{j} . \tag{14}$$

Equation 14 implies that the minority carrier transit time through the depletion region is short compared to the minority carrier lifetime and that the recombination losses of minority carriers photogenerated in this region are thus negligible.

# • Total Short Circuit Current Density

The total short circuit current density  $I_{sc}$  is found from the sum of short circuit current densities per unit wavelengths integrated over the relevant range of wavelengths:

$$I_{sc} = \int_{\lambda_{1}}^{\lambda_{2}} (I_{p} + I_{b} + I_{w}) d\lambda$$
 (15)

where  $I_p$ ,  $I_b$ , and  $I_w$  are given by Equations 9, 13, and 14. (The contribution  $I_D$  from the (AlGa)As window layer is included in the expression for  $I_p$  given by Equation 9.) The incident photon flux  $F(\lambda)$  included in the above equations is obtained from the AMO solar irradiance curve for sunlight outside the earth's atmosphere  $I_v$  (see References). The values of the absorption coefficient  $a(\lambda)$  used in Equations 9, 13, 14, and 15 were obtained from the documents referenced in Table 1. Some references give the imaginary part  $k(\lambda)$  of the index of refraction in lieu of the absorption coefficient  $a(\lambda)$ . The relationship between the two is  $a(\lambda) = 4\pi k(\lambda)/\lambda$ .

The calculations of  $R(\lambda)$ , which also appears in Equations 9, 13, and 14, were performed for the configuration shown in Figure 3. The values for the index of refraction  $n(\lambda)$  in these calculations were also obtained from the references of Table 1.

The following paragraphs and Figures 4 through 9 show the variation of  $I_{sc}$  calculated with Equation 15 as a function of a number of critical parameters.

# Diffusion Length

Figure 4 shows  $I_{sc}$  as a function of the electron diffusion length for three values of the junction depth:  $x_j = 0.2 \, \mu m$ ,  $1 \, \mu m$ , and  $2 \, \mu m$ . A hole diffusion length  $L_p = 2.0 \, \mu m$  is used in this calculation. The figure shows that for shallow junction ( $x_j = 0.2 \, \mu m$ ), the  $I_{sc}$  is independent of the electron diffusion length; for a deep junction solar cell, the  $I_{sc}$  is drastically reduced as the electron diffusion length decreases.

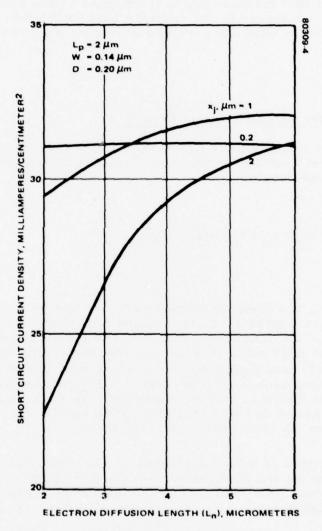


FIGURE 4. SHORT CIRCUIT CURRENT DENSITY VERSUS ELECTRON DIFFUSION LENGTH IN POSITIVE GAAS LAYER

Figure 5 shows  $I_{sc}$  as a function of the hole diffusion length in the n-GaAs layer for three values of junction depth  $(x_j=0.2~\mu m,~0.5~\mu m,~and~1~\mu m)$  with  $L_n=L_p$  and  $L_n=2~L_p$ , respectively. Comparison of Figures 5a and 5b again indicates that for the deep junction solar cell,  $I_{sc}$  is greatly reduced when the hole diffusion length is shortened. This observation is important where resistance to radiation damage is concerned. Because radiation damage leads to shorter diffusion lengths, the above results indicate the merits of relatively shallow junction depths (typically  $x_j \le 0.5~\mu m$ ).

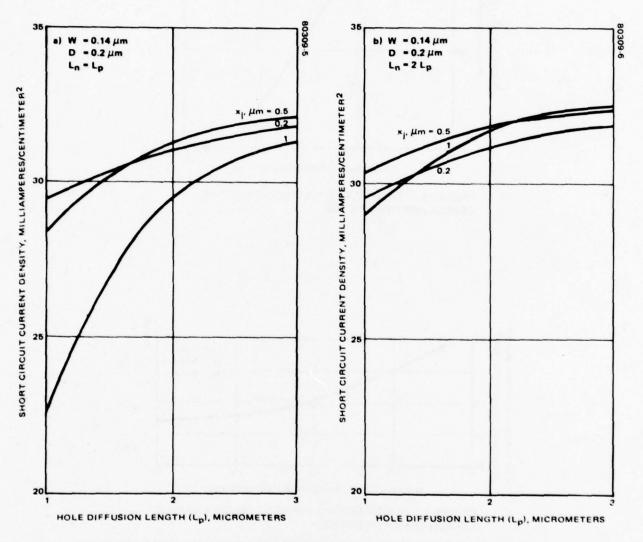


FIGURE 5. SHORT CIRCUIT CURRENT DENSITY VERSUS HOLE DIFFUSION LENGTH

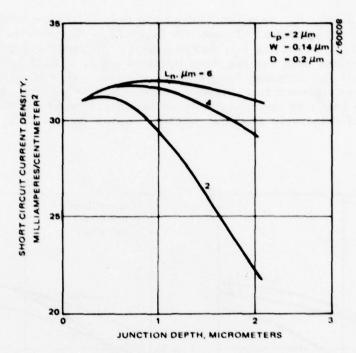


FIGURE 6. SHORT CIRCUIT CURRENT DENSITY VERSUS JUNCTION DEPTH

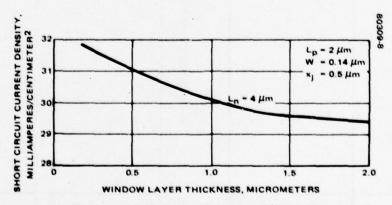


FIGURE 7. SHORT CIRCUIT CURRENT DENSITY VERSUS WINDOW LAYER THICKNESS

# Junction Depth

Figure 6 shows the short circuit current density as a function of junction depth for several values of electron diffusion length.  $I_{sc}$  reaches its peak value for an optimum junction depth  $\mathbf{x}_j$  and then decreases for greater depths. This optimum value depends on the diffusion length on both sides of the junction. The short circuit current density  $I_{sc}$  can be drastically reduced for deep junctions and short electron diffusion lengths as illustrated in Figure 5.

# Window Layer Thickness

Figure 7 shows the behavior of  $I_{SC}$  as a function of (A1Ga)As layer thickness for a representative case in which  $x_j$  = 0.5  $\mu m$ ,  $L_p$  = 2  $\mu m$ , and  $L_n$  = 4  $\mu m$ . It illustrates the substantial advantage of and strong incentive for using thin window (D<0.5  $\mu m$ ) layers.

# 2. OPEN CIRCUIT VOLTAGE (Voc)

In p-n junctions two dominant current transport mechanisms occur in parallel: the diffusion mechanism due to injection of carrier across the junction barrier and generation-recombination current within the depletion region. The diffusion current-voltage relationship for a forward bias can be expressed as

$$I_{diff} = I_{ol} (e^{qV/kT} - 1)$$
 (16)

where V is the voltage drop across the junction and  $\mathbf{I}_{\mathbf{S}}$  the saturation current density shown in Equation 17

$$I_{ol} = qn_{i}^{2} \left( \frac{D_{n}}{N_{A} L_{n}} \frac{S_{p} \cosh \frac{D + x_{j} + w}{L_{n}} + \frac{D_{n} \sinh \frac{D + x_{j} + w}{L_{n}}}{\frac{D_{n}}{L_{n}} \cosh \frac{D + x_{j} + w}{L_{n}} + S_{p} \sinh \frac{D + x_{j} + w}{L_{n}}} \right) + qn_{i}^{2} \left( \frac{D_{p}}{N_{D} L_{p}} \frac{S_{n} \cosh \frac{t}{L_{p}} + \frac{D_{p}}{L_{p}} \sinh \frac{t}{L_{p}}}{\frac{D_{p}}{L_{p}} \cosh \frac{t}{L_{p}} + S_{n} \sinh \frac{t}{L_{p}}} \right)$$

$$(17)$$

The first term on the right-hand side of Equation 17 is due to the electron injection into the base n region. The second term is due to the hole injection into the p region.

The generation and recombination current within the depletion region was treated by Shockley, Sah, and Noyce<sup>12</sup>. The maximum value of this current density is given by

$$I_{gr} = \frac{qn_{i} w}{\sqrt{\tau_{po} \tau_{no}}} \frac{2 \sinh\left(\frac{qV}{2kT}\right)}{q (V_{bi} - V)/kT} \frac{\pi}{2}$$
(18)

where  $\tau_{po}$  and  $\tau_{no}$  are the respective lifetimes of holes and electrons in the depletion region and  $V_{bi}$  is the built-in voltage of the p-n junction. The actual value of  $I_{gr}$  can be lower  $^{13}$  than that given by Equation 18.

The total diode current density is the sum of  $I_{\mbox{diff}}$  and  $I_{\mbox{gr}}$ . This can be approximated by

$$I = I_{ol} \left[ \exp\left(\frac{qV}{nkT}\right) - 1 \right]$$
 (19)

where n is a quality factor which varies between 1 and 2. The lower limit of n (n = 1) implies that the diode current is diffusion limited, while the upper value (n = 2) corresponds to the limiting case of generation-recombination. (Values of n > 2 are also possible if the space charge recombination process involves more than one intermediate energy level.)

The output current density of a solar cell under illumination, taking into account the series resistance  $R_{\mathbf{s}}$ , is thus given by

$$I = I_{sc} - I_{o} \left\{ exp\left(\frac{q}{nkT} \left(V + IR_{s}\right)\right) - 1 \right\}$$
 (20)

In the open circuit condition, the output current density is zero. Thus, the corresponding voltage  $(V_{\rm oc})$  is given by

$$V_{oc} = n \frac{kT}{q} \ln \left( \frac{I_{sc}}{I_{o}} + 1 \right)$$
 (21)

It can be seen that the series resistance does not affect the open circuit voltage. Equation 21 also implies that a high value of n would be desirable in obtaining high  $V_{\rm OC}$ . However, this is not the case, since high n implies high  $I_{\rm O}$  from Equations 16 through 19. Open circuit voltage for p-n junctions is always highest for the diffusion-limited case n=1. Thus, the

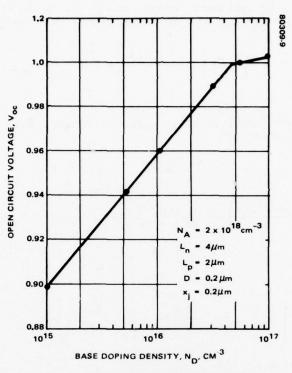


FIGURE 8. OPEN CIRCUIT VOLTAGE VERSUS BASE DOPING DENSITY

cell will produce the highest open circuit voltage when n = 1. Furthermore, high doping levels result in high  $V_{\rm OC}$ , as seen in Figure 8, in which  $V_{\rm OC}$  is plotted as a function of the n buffer layer doping level ND for the optimum case where n = 1.

#### 3. FILL FACTOR (FF) AND POWER CONVERSION EFFICIENCY $(\eta)$

Solar cells of quite different designs can deliver identical  $I_{\text{SC}}$  and  $V_{\text{OC}}$  and yet may still differ in their power conversion efficiency because of different forward current-voltage characteristics. This is because the current-voltage relationship does not have an absolutely square "knee." The actual maximum power output,  $P_{\text{max}}$ , of the cell will always be less than the product of  $I_{\text{SC}}$  and  $V_{\text{OC}}$ . A convenient figure of merit to describe this effect is the fill factor (FF) defined by

$$FF = \frac{P_{\text{max}}}{I_{\text{sc}} V_{\text{oc}}}$$
 (22)

Any effect which tends to soften the knee of the diode I-V characteristics will reduce FF and hence reduce the power output from the solar cell. The output power (Pout) of a solar cell under illumination is given by

$$P_{out} = VI = I \frac{nkT}{q} \ln \left(1 - \frac{I - I_{sc}}{I_o}\right) - I^2 R_s$$
 (23)

The maximum power output,  $P_{max}$ , occurs at a current  $I_m$ ; it is obtained by setting dP/dI = 0.

Thus,

$$\frac{nkT}{q} \ln \left( 1 - \frac{I_{m} - I_{sc}}{I_{o}} \right) = I_{m} \left[ \frac{nkT}{q} \frac{1}{I_{o}} - \frac{1}{I_{m} - I_{sc}} + 2 R_{s} \right]$$
(24)

and

$$P_{\text{max}} = I_{\text{m}} \left[ \frac{nkT}{q} \ln \left( 1 - \frac{I_{\text{m}} - I_{\text{sc}}}{I_{\text{o}}} \right) - I_{\text{m}}^{2} R_{\text{s}} \right]$$
(25)

Using Equation 22, this fill factor is

$$FF = \frac{I_{m} \left[ \frac{nkT}{q} \ln \left( 1 - \frac{I_{m} - I_{sc}}{I_{o}} \right) - I_{m}^{2} R_{s} \right]}{I_{sc} V_{oc}}$$
(26)

The power efficiency of a solar cell in converting light of any arbitrary spectral distribution into useful power is given by

$$\eta = \frac{V_m I_m}{P_{in}} = \frac{FF \times V_{oc} \times I_{sc}}{P_{in}}$$
 (27)

Table 2 shows the calculated values for fill factor FF and power efficiency  $\eta$  for various values of series resistance  $R_s$ . The parameters used to calculate the short circuit current density  $I_{sc}$  and the reverse saturation current density  $I_o$  are D = 0.2  $\mu m$ , xj = 0.2  $\mu m$ , Ln = 2Lp. NA = 2 x  $10^{18}$  cm $^{-3}$ , ND = 1 x  $10^{17}$  cm $^{-3}$ , Sa = 1 x  $10^6$  cm/sec, Sp = 1 x  $10^4$  cm/sec, Sn = 1 x  $10^3$  cm/sec, and n = 1. (Note that I is a current density and that to obtain voltage units the  $R_s$  is really ohm-cm $^2$ . The data in Table 2 are thus normalized to 1 cm $^2$  area solar cell.)  $R_s$  must be larger than 0.3 ohm-cm $^2$  (or 0.075 ohm for a 4 cm $^2$  solar cell) before an appreciable decrease in FF is noticeable.

TABLE 2. FF AND  $\eta$  FOR SEVERAL DIFFERENT VALUES OF SERIES RESISTANCE\*

$R_{s'} \Omega$ -cm <sup>2</sup>	Lp	V <sub>oc</sub> , Volts	A/cm <sup>2</sup>	I <sub>sc</sub> , mA/cm <sup>2</sup>	I <sub>m</sub> , mA/cm <sup>2</sup>	P <sub>m</sub> , mW	FF	η, %
0	1	1.0	5.47 x 10 <sup>-19</sup>	31.3	30.43	27.70	0.885	20.46
	2	1.02	2.7 x 10 <sup>-19</sup>	31.8	30.93	28.72	0.885	21.2
	3	1.03	1.8 x 10 <sup>-19</sup>	31.8	30.93	29.04	0.887	21.4
0.3	1	1.0	5.41 x 10 <sup>-19</sup>	31.3	30.43	27.42	0.876	20.2
	2	1.02	2.7 x 10 <sup>-19</sup>	31.8	30.93	28.41	0.876	20.9
	3	1.03	1.8 x 10 <sup>-19</sup>	31.8	30.93	28.76	0.878	21.2
1.0	1	1.0	5.41 x 10 <sup>-19</sup>	31.3	30.38	26.78	0.856	19.7
	2	1.02	$2.7 \times 10^{-19}$	31.8	30.89	27.76	0.856	20.5
	3	1.03	1.8 x 10 <sup>-19</sup>	31.8	30.89	28.09	0.857	20.7
3	1	1.0	5.41 x 10 <sup>-19</sup>	31.3	30.22	24.94	0.797	18.4
	2	1.02	2.7 x 10 <sup>-19</sup>	31.8	30.74	25.86	0.797	19.1
	3	1.03	1.8 x 10 <sup>-19</sup>	31.8	30.74	26.18	0.799	19.3
6	1	1.0	5.41 x 10 <sup>-19</sup>	31.3	29.92	22.23	0.710	16.4
	2	1.02	$2.7 \times 10^{-19}$	31.8	30.41	23.06	0.711	17.0
	3	1.03	1.8 x 10 <sup>-19</sup>	31.8	30.45	23.38	0.714	17.2
10	1	1.0	5.41 x 10 <sup>-19</sup>	31.3	29.15	18.73	0.598	13.8
	2	1.02	2.7 x 10 <sup>-19</sup>	31.8	29.68	19.43	0.599	14.3
	3	1.03	$1.8 \times 10^{-19}$	31.8	29.71	19.74	0.603	14.58

<sup>\*</sup>Assuming no shadowing.

The upper limit to  $I_{\rm SC}$  is determined by the bandgap of the semiconductor. For the GaAs solar cell it is 37 mA/cm for AMO spectral condition. This upper limit occurs when every incident photon creates an electron hole pair which is subsequently collected by the p-n junction. The corresponding theoretical upper limit for power conversion efficiency is 24 percent using a fill factor of 0.88 and an open circuit voltage of 1 volt. The actual calculated efficiency in Table 2 is lower than the upper limit. This discrepancy is due to the losses in the bulk and surface recombination in different regions of the cell, which are reflected in the parameters used for calculations seen in Table 2.

Figure 9 shows a sample calculation of power efficiency as a function of base diffusion length for different values of series resistance used in Table 2. In this calculation we assume n=1 and window layer thickness 0.2  $\mu$ m. Table 3 provides the experimental data for cell 373, whose 1-V curve is plotted in Figure 10. From Figure 10 and the data in Table 3, it is seen that Rs can be less than 0.075 ohm for a cell area of 4 cm<sup>2</sup> and that the contract goal of 18 to 20 percent efficiency at AMO is a realistic goal for a 4 cm<sup>2</sup> cell.

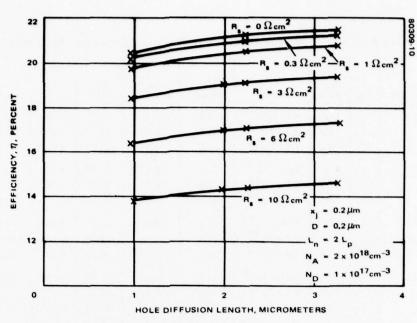


FIGURE 9. POWER CONVERSION EFFICIENCY (  $\!\eta\!$  ) VERSUS BASE DIFFUSION LENGTH (L  $_p$  )

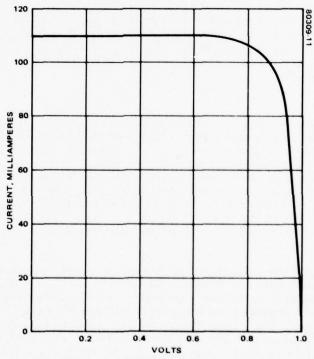


FIGURE 10. AMO CURRENT VERSUS VOLTAGE OF (AIGa)As-GaAs SOLAR CELL (CELL NO. 373)

# TABLE 3. EXPERIMENTAL DATA FOR $(Al_{x}Ga_{1\cdot x}) = Ga|Al$ SOLAR CELL NO. 373

Area of cell	A	=	4 cm <sup>2</sup>
$X \text{ in } Al_X Ga_{1-X} = 0.9$			
$N_A = 10^{18} cm^{-3}$			
Window layer thickness	D	=	0.8 <sub>m</sub> m
Base doping	$N_D$	=	2 x 10 <sup>16</sup> cm <sup>-3</sup>
Open circuit voltage	Voc	=	1 V
Short circuit current (with glass)	ı <sub>sc</sub>	-	106 mA
Current max	1 <sub>m</sub>	-	100 mA
Voltage max	Vm	=	0.88 V
Fill factor	FF	=	0.83 V
Series resistance	$R_s$	=	0.067 Ω
Junction perfection factor	n	=	2.10
Diode leakage current	lo	=	1 x 10 <sup>-9</sup> A
Power conversion efficiency	0	=	16.3%

Cell 373 is somewhat different than the base line cell in Figure 11 since it was fabricated to study the influence of on carrier concentration in the buffer layer.

#### SECTION III

# GaAs SOLAR CELL BASELINE DESIGN

An evaluation of the theoretical model and the cell structure led to the choice of the baseline design for the GaAs solar cell shown in Figure 11. The  $\rm n^+$  concentration for the substrate was fixed at 5 x  $10^{17}$  cm<sup>-3</sup> and Te was selected as the dopant. The reason for this choice is that the substrate has been developed to a high degree for use in LEDs, and it provides the most economical choice for the solar cell until we can establish the optimum concentration in the buffer layer for the n side at the active junction. In the future we may eliminate the need for one epitaxial growth of a buffer layer by adequate improvement in bulk growth. The highly doped substrate also makes contacting with Au-Ge-Ni considerably easier.

For the cells to be fabricated the n buffer layer concentration was fixed at  $1\times10^{17}~cm^{-3}$ . This value was chosen in the light of results on the variation of open circuit voltage as a function of carrier concentration in the n layer. At this doping level we have about 1 volt, and further increase in n concentration seems to adversely affect short circuit current. We chose it as the best compromise for short circuit current and open circuit voltage control of epitaxial layer growth on tin-doped substrates. The thickness of this layer was fixed at 10  $\mu m$  or more because results indicated that the substrate "visibility" is minimized at a buffer layer thickness of 10  $\mu m$ . A lesser thickness is not always sufficient to remove the effect of the substrate on cell performance. It is worth noting that this thickness is about three times the minority carrier diffusion length.

The p (AlGa)As window layer thickness, D, is chosen for the present design to be  $\leq 0.5 \, \mu m$  because it is relatively easy to control the liquid phase epitaxy (LPE) layer thickness at this value over the large areas necessary for the solar cell. It is also a convenient dimension in terms of growth time, which effectively determines the junction depth in the finished structure. During later stages of the program, we fine tuned this parameter to even lower values.

The p-GaAs layer, formed by the diffusion of Be into the grown LPE n-type buffer layer, is controlled in thickness by the diffusion time and temperature. In practice, it seems to be controlled by the time and temperature of epitaxial growth of the (AlGa)As layer (Section VI). The p GaAs thickness (junction depth, xj) is an extremely important parameter for radiation damage control and is therefore crucial to space cell performance. Optimization of this parameter constituted a principal activity of the second phase of the program.

The remaining parts of the baseline structure are self-expanatory. The Au-Zn contacts are about 3000 to 4000 Å with a silver overlay about 4  $\mu m$  thick; the n contact is Au-Ge-Ni (~5000 Å) with an Ag overlay. The antireflection coating is 600 Å of Ta<sub>2</sub>O<sub>5</sub> and is the same as that used in silicon space cells, except that the thickness is optimized to match the spectral response of the GaAs cell. The cells delivered to the Air Force Aero Propulsion Laboratory were based on the design shown in Figure 11.

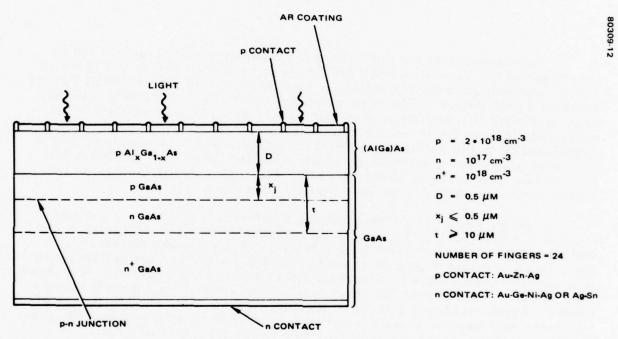


FIGURE 11. GaAs SOLAR CELL BASELINE DESIGN

#### SECTION IV

# EXPERIMENTAL CELL FABRICATION AND RESULTS

#### 1. CELL FABRICATION

At the beginning of the GaAs solar cell program, several choices had to be made among the alternative fabrication techniques available. On the basis of the Hughes Research Laboratories (HRL) experience, we chose to use the infinite melt epitaxial growth technique for the device structure, a mechanical mask, Au-Ge-Ni and Au-Zn alloys for the contacts, and Ta<sub>2</sub>O<sub>5</sub> for the AR coating. The reasons for these choices and their advantages are described below.

# Liquid Phase Epitaxy Growth

The basic building block of the GaAs solar cell is an (AlGa)As-GaAs structure grown by liquid phase epitaxy (LPE), since the best results for cell performance have been obtained using this method. Of the two best known variants, the limited melt 14 and the infinite melt techniques, we chose the HRL-developed infinite melt technique for its ability to reproduce large area cells with superior performance. The advantages of this technique have been discussed in several publications. 15, 16, 17

Briefly, the limited melt technique suffers from a large surface-to-volume ratio for the growth solution, which makes contamination of the solution difficult to control. This factor becomes especially important in the light of thermal cycling test results showing the adverse effect on cells of oxygen contamination (see Section VII). The limited melt technique is also disadvantageous from the standpoint of the economics of cell production. It cannot use the Ga solution efficiently because the wiping technique used at the end of epitaxial layer growth results in unavoidable losses.

By contrast, HRL has used a 1000 g Ga solution for a period of 2 years to produce over 1000 cells, and the solution has, if anything, improved in purity and reproducibility over that period of time. Solar cells with areas of 4 cm² have been reproducibly and routinely fabricated with AMO efficiencies in excess of 15 percent, and we have demonstrated that this technique can be used to grow even larger area cells. We are presently setting up a system under the High Efficiency Solar Panel (HESP) program that will enable us to grow eight cells at a time, making the economics of cell production extremely attractive.

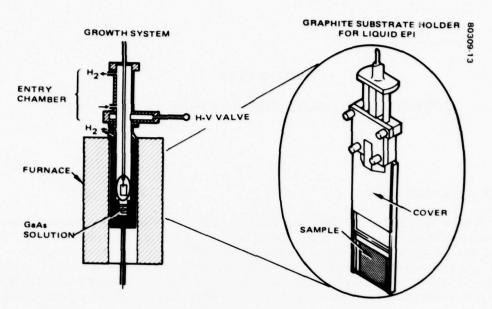


FIGURE 12. INFINITE MELT LIQUID PHASE EPITAXIAL GROWTH OF GaAs

The basic LPE system developed at HRL is shown in Figure 12. It features an all-quartz growth tube connected to a stainless steel entry chamber through a high vacuum valve. A solution of high purity GaAs in either Ga or a mixture of Ga and Al serves as the growth solution. The Al to Ga ratio can be adjusted to give any composition from GaAs to AlAs for the epitaxial layer, and dopants such as Te, Sn, Ge, or Be can be used to produce a variety of doped layers. Once a solution is prepared it is maintained in a pure Pd crucible, diffused hydrogen ambient at close to the growth temperature for periods of months while layers are grown. Additional details about the system can be obtained from other publications. 15, 16

Layers have been reproducibly grown from the system with thicknesses down to 0.5  $\mu$ m with a variation in thickness of less than  $\pm 10$  percent over substrates larger than 6 cm<sup>2</sup> in area. The surfaces are specular and can be processed as grown for devices. Since a growth run takes only about an hour, the system can be adapted for large scale production of low cost cells.

A substrate holder (Figure 12) is used to ensure good equilibration between the substrate and the growth solution prior to the start of growth. It enhances the capability of the HRL infinite melt system for the growth of strain-free large area layers with a uniformity in carrier concentration and thickness that would be difficult without it.

We have discovered that the variability of commercially available GaAs substrates results in serious differences in the quality of the cells. To eliminate this problem we have adopted the method of growing an n-type

buffer layer with a controlled n-type concentration provided by a tin-doped GaAs solution. The method also enables us to study the variations in cell performance as a function of the carrier concentration in the n-type layer. Tin has turned out to be an excellent dopant with low vapor pressure and well behaved segregation coefficients. We have tried Te as an alternative dopant. Because of its somewhat larger vapor pressure we have, however, favored tin in most of our studies.

#### Contacts

Once the basic epitaxial structure was available, the next important requirement for cell fabrication was a method of making reliable ohmic contacts. One of the major problems encountered by previous workers was making ohmic contacts that would adhere to (AIGa)As.

Contacts to semiconductors are empirical at best. One or more metals are applied to the semiconductor surface with a dopant and a fluxing transition metal such as Ni, Cr, Pd, or Ti. For the n GaAs such contacting systems are available. Au-Ge-Ni and Au-Sn are good examples, the former for a 450°C contact and the latter for one with somewhat higher temperature capability (600°C). We chose Au-Ge-Ni as our first candidate since it is compatible with the Au-Zn system for the p-type material; the latter has been most often used for p-type GaAs contacts.

Having chosen the alloys, the next question was the best technique of metallization for optimum results. The two most commonly used methods are evaporation (either thermal or E-beam) and sputtering (RF or dc using ion beams). The evaporation method implies high temperatures, and since the metals are so different in vapor pressures (Zn-Au), we believed sputtering would have some advantages in control. We therefore concentrated on sputtering as the main approach during the first phase of the program.

The last choice in contacts is with respect to the production of the contact grid pattern on the p side. The typical grid pattern we use is a 24 finger pattern (Figure 13). It is a good compromise for minimum shadowing (~5 to 8 percent) and has good collection efficiency. We could obtain the pattern using either photolithography or mechanical masks. HRL is developing both techniques concurrently for use in a variety of applications. For a cell compatible with concentrated illumination, the photolithographic technique is especially useful, since it provides the high resolution necessary for the closely spaced contact pattern required to minimize series resistance in high current operation. However, for high efficiency cells at low concentrations a mechanical mask approach offers a simpler technique that is compatible with silicon solar cell practice, which is a significant factor in establishing a rapid transition to production for GaAs solar cells. We accordingly concentrated on the mechanical mask approach and the standard 24 finger mask used by Spectrolab for silicon 2 x 2 cm space cells.

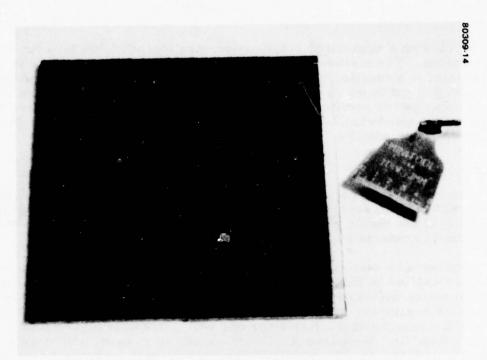


FIGURE 13. 2 X 2 CM GaAs SOLAR CELL WITH FRONT GRID PATTERN

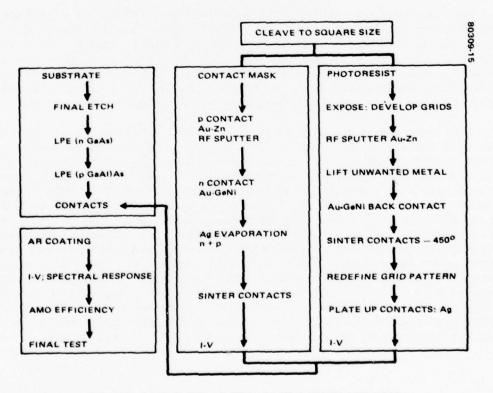


FIGURE 14. GaAs SOLAR CELL FABRICATION AND TEST

## Antireflection Coating

The antireflection (AR) coating chosen was Ta<sub>2</sub>O<sub>5</sub>. We tried other materials such as  $TiO_{\mathbf{x}}$ , zirconium silicate, and oxides of silicon, but saw no clear advantage in departing from the tantalum oxide which is presently space qualified for silicon cells.

# Cell Fabrication Flow Chart

The flow chart for cell fabrication and test is shown in Figure 14. It is worth noting that the mechanical mask alternative has fewer steps compared to the photoresist process for contacting the cells.

#### 2. RESULTS

# Liquid Phase Epitaxy

# Reproducibility and Role of the Substrate

The capability of the HRL infinite melt technique can best be seen from the characteristics of the cells fabricated by this process. Tables 4, 5, and 6 give the solar cell characteristics at three stages in our solar cell program, the first two showing the cells fabricated prior to the present contract and the last showing the status of the cells at the beginning of 1977 at the end of 5 months of the present contract. The cell numbers in the first column give the chronological order in which the layers were grown; each set contains a group of cells that were processed together for contacting in one eight-cell mask. The reproducibility in  $I_{\rm SC}$  and  $V_{\rm OC}$  is striking in all cases. Even at the earliest stages of the program (Table 4) the cells behaved predictably. It is worth noting that cell 88 has lower efficiency than the others. In several other experiments of a similar nature, we noticed that when the commercial substrates of Te-doped GaAs were used, the efficiency was not consistent and was often lower than that for cells in which epitaxially grown buffer layers were used.

In this regard, it has been the practice in some laboratories 14 to use a "leaching" method to getter or leach out impurities by using a saturated Ga solution to improve substrate quality. Improved efficiency has then been observed in these GaAs cells. The technique, however, should be considered a demonstration of the need to improve substrates rather than a production tool, since it involves very careful and time-consuming procedures. Furthermore, the leaching tends to contaminate the solution since it cannot be used too many times without lowering its ability to getter the impurities. The cost of Ga precludes such a procedure. Growth of the epitaxial buffer layer with the optimum n-type concentration eliminates the need for gettering. It also permits the reproducible control of the n-layer composition. This is important during the early phases of cell development, when we are trying to quantitatively establish the significance of the n layer composition for cell performance. Table 5, which presents the data for eight cells, demonstrates the strength of this approach. These cells had the same n layer

TABLE 4. HRL GaAs SOLAR CELL CHARACTERISTICS: JANUARY 1976

Cell No.	$N_{\rm D} \times 10^{17}  {\rm cm}^{-3}$	D, μm	I <sub>sc</sub> , mA	V <sub>oc</sub> , mV	η (AMO)	FF
81	1	1.5	99	1000	13.6	73
82	1	1.5	99	1000	14	76
83	1	1.5	99	1000	14.9	80
84	1	1.5	99	1000	14	74
85	1	1.5	100	990	14.1	77
86	Broken					
87	8*	2	(Le	aky)		
88	8*	1.3	89	950	12.9	73

\*Substrate with no buffer layer

TABLE 5. HRL GaAs SOLAR CELL CHARACTERISTICS: JUNE 1976

Cell No.	I <sub>sc</sub> , mA	v <sub>oc</sub> , v	Efficiency, %	FF
287	110	0.98	15.5	0.78
288	110	0.98	15.7	0.80
289	107	0.98	15.5	0.80
290	110	0.98	15.5	0.78
291	110	0.98	15.5	0.78
292	110	0.98	15.5	0.78
293	111	0.98	15.7	0.80
294	110	0.98	15.7	0.79

Cell size: 2 X 2 cm; At level (X) = 0.97Be doping (AlGa)As  $> 3 \times 10^{18}$  cm<sup>-3</sup>

 $N_D = 1 \times 10^{17} \text{ cm}^{-3}$ 

TABLE 6. HRL GaAs SOLAR CELL CHARACTERISTICS: JANUARY 1977

Celi No.	$N_D \times 10^{17} \text{ cm}^{-3}$	D, μm	I <sub>sc</sub> , mA	V <sub>oc</sub> ,V	η (AMO)	FF
522	0.04	0.4	115	0.90	15.9	0.83
524	0.04	0.4	116	0.90	16.2	0.83
525	0.04	0.4	116	0.90	15.9	0.82
523	0.3	0.4	118	0.98	17.5	0.82
526	0.3	1	110	0.98	17.2	0.86
527	0.3	1	109	0.98	16.9	0.85
529	0.3	2	106	0.98	16.1	0.82

concentration and p layer thickness. The amazing reproducibility of cell parameters is the best justification for the HRL approach to cell fabrication.

Table 6 demonstrates the continuing improvement of cell properties during the present contract. Several factors are shown by the results. Cells 522, 524, and 525 have the same n layer carrier concentration. Their open circuit voltages and short circuit currents are very similar. The performance of cells 523, 526, 527, and 529 varies systematically (as would be expected from theory) as a function of p-GaAs layer thickness  $(x_j)$  and carrier concentration. The open circuit voltage further increases as a function of n layer carrier concentration in the two sets of samples. Finally, the cell fill factors are the highest noted in the available literature.

Since the 17.5 percent efficiency was achieved, the emphasis was shifted to increasing the radiation resistance of the cell. In our latest cells, these desirable goals are achieved without loss of efficiency. The steps that led to these improvements in cell modeling and processing are treated below in detail.

Best solar cell performance is obtained if a double LPE layer growth is used. The layer carrier concentration for both the n and p layers requires optimization, but the trends are clear. The cells grown according to the growth schedule in Tables 5 and 6 were used for radiation damage studies and showed degradation in close agreement with calculated values (see Figure 40, Section VI) for cells with junction depth  $\sim 0.8$  to 1  $\mu$ m. Since resistance to radiation damage is an important consideration for space applications, we had to modify the growth schedule for the GaAs solar cells to achieve the necessary junction depth control.

The factors that control junction depth are 1) the Be concentration in the growth solution, 2) the growth parameters involving nucleation, and 3) the time of growth. The study of these factors required modification of the Be concentration in the growth solution. A systematic study of the growth temperatures and cooling cycles used for growth also was needed.

Be Concentration in Growth Solution - There were a few surprising developments in the use of Be as a dopant during the course of this study. When the amount of Be in the solution was increased, we noted that the increase in the layer concentration was not proportional. Increasing Be concentration in the solution by a factor of 5 above that required for 1 x 10<sup>18</sup> cm<sup>-3</sup> carrier in the epitaxial layer increased the layer concentration by less than a factor of 2. We had, therefore, to conclude that the stability of Be in the solid layer reaches a saturation somewhere about 1.5 x 10<sup>18</sup> cm<sup>-3</sup> and is insensitive to increased Be concentration in the solution adversely affects the layer by increasing the junction depth. Our studies indicated that the solution acts as a diffusion source with higher Be, increasing junction depth without increasing the concentration in the solid layer.

The junction depth is especially sensitive to the solution concentration when slow growth rates are used and the (AlGa)As forms slowly, thus increasing the time for which the GaAs can "see" the high Be concentration in the solution. Once a continuous layer a few hundred angstroms thick forms on the GaAs, the influence of Be in the solution on junction depth is limited. The initial rapid diffusion of Be (see Figure 24, Section V) can be attributed to the time during which the solution sees the GaAs. Two conclusions were drawn from these observations:

- a) Increase of Be in the solution beyond that needed to give ~1.5 x 10<sup>18</sup> cm<sup>-3</sup> in the solid is harmful to controlled growth. This finding is additionally desirable to minimize the possible harmful effects of Be in processing.
- b) The epitaxial layer growth cycle should minimize the contact of the solution to the GaAs substrate during initial nucleation and growth of the layer to reduce junction depth; further, the lower the temperature of growth, the shallower the diffusion will be.
- 2) Influence of Growth Parameters - The influence of the temperature of growth on diffused junction depth is obvious. However, what is not obvious is the influence of the solution concentration in Be on the junction depth (see item 1 above). The values of junction depth shown in Tables 14 and 15 (Section V) substantiate the conclusions from item 1. The fact that increasing epitaxial growth time increases junction depth only very slowly again shows the overwhelming influence of the solution during the initial seconds. The importance of this finding becomes obvious if we wish to use a solution etch prior to growth of the layer, a practice sometimes recommended by other workers to improve layer perfection. Such a procedure would expose the substrate to the solution for appreciably longer time, thus increasing the junction depth. Since we have established the importance of a shallow junction in reducing radiation damage, it becomes evident that this desirable objective can only be met by either reducing the Be concentration in the solution to the minimum necessary for cell performance or by minimizing the nucleation time so that the grown layer offers an effective barrier to diffusion from the solution. Use of these two approaches in combination has enabled us to reduce the junction depth to less than  $0.5 \, \mu m$ .
- 3) Growth Time The influence of the epitaxial layer growth time on junction depth was discussed in part under item 2 above. To reduce junction depth, it would be desirable to reduce growth time as well as nucleation time. It is important, however, that the growth rate be slow enough to allow for orderly growth of the layer to maintain good crystal perfection as well as dopant

segregation at the growth interface. Besides these limitations, there are also practical considerations of cooling large volumes of solution while using a heavily insulated furnace when cooling rates exceed several degrees per minute. The growth temperature of 800°C imposes a practical limit of approximately 2°C/min without resort to forced cooling. In our experiments we find that a good compromise for GaAs solution in Ga is somewhat below 1°C/min, the exact rate being dependent on the system geometry, dopant type, and concentration. This enables us to grow an epitaxial layer at about 1 µm/min; a buffer layer about  $10~\mu m$  thick can then be grown in 10~minutes. The (AlGa)As layer is grown at a much slower rate since we have to obtain thickness control in the 0.4 µm range. At a growth temperature of 800°C, a cooling rate of ~0.3 deg/min has given us a 2000 Å layer per minute. The growth rate for the (AlGa)As layer is considerably slower because the solute concentration is lowered as we go to AlAs from GaAs at comparable temperatures. Thus, at 800°C we have approximately a 2 percent solution in (AlGa)As compared to a 5 percent solution in GaAs. Since slow growth rates have to be used to achieve reproducible layer thickness in the submicron window layer growth, it becomes imperative to keep down the Be concentration to reduce junction depth.

By combining the considerations discussed above, we were effectively able to reduce the junction depth of the GaAs cell below the heterophase boundary of the window layer to less than  $0.5 \,\mu m$ . The improvement in radiation damage so achieved can be seen in Figure 42 (Section VI).

An examination of the cell efficiencies in Table 16 (Section V) shows that 17.5 percent efficiency at AMO was achieved in January 1977. Since then, the cells have not exceeded this figure, even though several improvements have been achieved in contact integrity, cell reproducibility, and improved process control, resulting in better overall device yield. The main reason for this result is the concentration of our efforts in reducing junction depth. However, as the junction gets shallower, two problems arise. First, the heterophase boundary (AlGa)As-GaAs gets closer to the electrical junction. This effectively reduces junction quality because the heterophase boundary is somewhat more strained and tends to have a lower minority carrier diffusion length region close to it. Second, as we reduce the window layer thickness, the electrical junction also gets closer to the top surface of the cell, where the metallic contacts that have to be annealed are located. Metals in the contacts are susceptible to migration and diffusion, both effects being enhanced by the strained heterophase region. As we tried to modify the processing parameters to control junction depth, these problems had to be studied and solutions found for them in parallel. Since very little is known about the characteristics of (AlGa)As with higher than 85 to 90 percent Al, progress was slow. However, by slowing the growth of epitaxial layers, we were able to minimize the adverse effects of the heterophase boundary and to fabricate the solar cells from structures

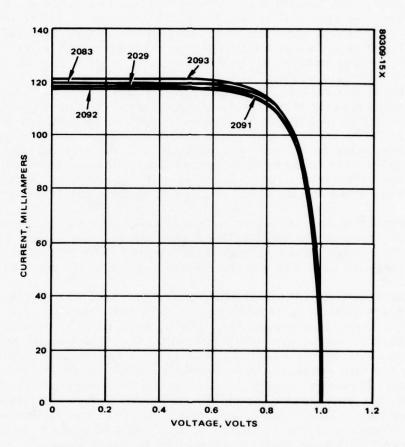


FIGURE 15. TYPICAL PHOTO I-V CHARACTERISTICS FOR CELLS IN TABLE 7

with junction depths less than  $0.5 \, \mu m$ . The improvements in the cell characteristics can best be seen with steady improvement in the fill factor from < 0.75 to 0.78 to 0.8. It is worth noting that the deep junction cells (520 to 527) had fill factors as high as 0.86. We believe further improvement in layer quality will enable us to reestablish these higher values even with shallower junctions.

The combined effect of these investigations led to cells with the characteristics shown in Table 7. AMO efficiencies are once again in the 17 percent range, even though the cells are grown using the new processing techniques with window layers and junction depth parameters suitable for higher radiation resistance. The processing reproducibility and cell yields improved considerably, and the contacts do not peel as easily as they did in our earlier cells. The open circuit voltages are consistently above 1 volt, and the short circuit currents are above 110 mA. The photo I-V characteristics of these cells are given in Figure 15. Comparison with Figure 33 (Section V) shows the similarity in characteristics with the earlier cells with the deeper junction.

# Role of Oxygen in Liquid Phase Epitaxy Layer Characteristics

During the course of the program, we studied the influence of oxygen in the growth ambient on cell performance. It is known from the literature that oxygen acts as a deep donor in GaAs and therefore affects its electrical characteristics. It should have a similar role in (AlGa)As, although its exact behavior is not known; it can act in different ways. For example, it

TABLE 7. (AIGa) As-GaAs SOLAR CELL CHARACTERISTICS (AMO)\*

Cell No.	l <sub>sc,</sub> mA	V <sub>oc,</sub> V	FF	η,
1960	116	1.01	0.76	16.5
1966	116	1.01	0.76	16.5
2029	118	1.02	0.76	16.9
2083	120	1.01	0.76	17.1
2087	113	1.02	0.78	16.7
2089	112	1.02	0.78	16.4
2090	113	0.99	0.77	16.0
2091	117	1.02	0.78	17.0
2092	118	1.02	0.78	17.4
2093	121	1.01	0.76	17.2

<sup>\*</sup>Delivered to AFAPL June 1978. Cell size = 2 X 2 cm<sup>2</sup>; buffer layer carrier conc N = 1 X 1017 cm<sup>-3</sup>.

can combine with silicon normally present as an impurity in the growth system to form SiO<sub>2</sub>, which is inactive and therefore reduces the silicon level in the grown layer. Alternatively, it can compesate for the shallow acceptor levels and therefore affect the carrier balance in the GaAs.

At one point in the program, one of the epitaxial growth systems developed a leak, and we noticed a serious deterioration in the performance of the solar cells. Simultaneously, we discovered a roughening of the grown surface and an abnormal increase in the number of dislocations in the epitaxial layer. We accordingly carried out a detailed investigation of the influence of traces of oxygen on epitaxial layer properties. Any increase of oxygen above 10 PPM resulted in visible and extensive surface deterioration; even traces in the PPM range affect the Hall mobility of the (AlGa)As layer. Table 8 shows a typical set of values obtained during this period. The results seem to indicate that oxygen acts as a compensating deep donor in (AlGa)As, with a severe reduction of the Hall mobility even in layers doped as high as  $1018~\rm cm^{-3}$  with Be.

Since the influence of oxygen on the layer quality has been demonstrated, we have installed an oxygen monitor (Research, Inc. oxygen monitor with range extender) that can measure oxygen concentration down to 0.2 PPM in the H2 flowing through the system. The oxygen levels are kept below 0.5 PPM throughout the epitaxial layer growth cycle. Our investigations have shown that this measure is especially important for ensuring the reproducibility of the window layer of (AlGa)As.

Another factor of critical significance to the reproducibility of the layer characteristics is the quality of deionized water used to clean the GaAs substrates and finished grown structures. When the water quality falls below 10 to 12 megohms, the grown layers begin to evidence surface problems: roughness, and an increased tendency to retain gallium on

TABLE 8. ROLE OF OXYGEN IN (AIGa)As LAYERS: ELECTRICAL CHARACTERISTICS

	Hall Measure	ement Values		
Date Grown	Carrier Concentration, Hall Mobil cm <sup>2</sup> V·1 sc		Remarks	
8 Dec 1976 17 Jan 1977	2 x 10 <sup>18</sup> 2 x 10 <sup>18</sup>	108 117	<ul> <li>Prior to oxygen leak cells with efficiency 16 to 17% (AM0)</li> </ul>	
6 Apr 1977	7.7 x 10 <sup>17</sup>	48	<ul> <li>After leak started</li> <li>Cells show poor efficiency, &lt; 14%</li> </ul>	
23 May 1977	2 x 1018	114	<ul><li>Leak fixed</li><li>Mobility recovers</li><li>New cells show better efficiency</li></ul>	

spots, with a subsequent increase in oxidation of the surface at these spots. Especially with the large area cells, it is important to avoid this problem to obtain high enough yields in cell production. Besides the deionized water, all organic chemicals such as isopropyl alcohol, freon, and similar solvents used must be meticulously kept free of dust particles and moisture, since these tend to cause tailing of Ga on the substrate surface and subsequent irregular growth. Besides the problems in epitaxial growth, the lack of care in handling, deterioration of water or solvent quality, or undue exposure to humidity or dusty air, can lead to severe adhesion problems in the grid contacts on the p (Al-Ga)As layer. Some contact peeling in our early cells has been traced to these problems.

### Contacts

Tables 4, 5, and 6 show that the contacts to (AlGa)As layers using Au-Zn are satisfactory. However, our experience has been that these contacts exhibit erratic behavior. While some sets of cells have excellent ohmic contacts, others tend to have serious nonohmic components, as shown by the I-V curves. A systematic study of the contact problem established the reasons for the erratic behavior. There are three principal reasons for the failure of Au-Zn contacts to (AlGa)As:

- 1) The refractory native oxide layer on (AlGa)As acts as a barrier layer, preventing ohmicity.
- The extremely high vapor pressure of zinc makes controlled deposition of Au-Zn by evaporation of the alloy difficult.
- 3) The control of the stoichiometry of Au-Zn is especially critical at the semiconductor surface.

The use of a low temperature sputtering process eliminated the problems associated with items 2 and 3. The last batches of cells made have reproducible characteristics, demonstrating that such reproducibility can be obtained by carefully preventing any temperature rise in the deposition system. The problem arises principally because zinc has a high vapor pressure at temperatures as low as 100°C, and the sticking coefficient of zinc to (AlGa)As is quite low once the temperature rises. Since an alloy of about 5 to 8 percent Zn is used for sputtering, it is important that all temperatures in the system be maintained low, especially if fairly long deposition times are used. Increasing the amount of zinc in the starting alloy causes problems because of zinc oxide formation and large deposits of zinc in the bell jar.

The increased temperature in the deposition system is also undesirable because it causes oxide formation at the (AlGa)As surface. We succeeded in minimizing the oxide formation by better handling procedures and limiting temperature excursions on the surface. Once the processing is finished and the contacts are annealed at 500°C, the oxide formation problems seem to be eliminated.

We also established a simple way to eliminate all traces of the oxide just prior to the Au-Zn contact deposition by backsputtering about 100 Å in the contacting system. Extreme care has to be taken, however, to ensure that the sputtering system is oxygen-free, since traces of oxygen cause an oxide formation on the virgin sputtered surface very rapidly.

We investigated the possibility of using photolithography as an alternative to mechanical masks. The method is attractive because of the high resolution obtainable and because it enables us to contact the GaAs directly rather than the (AlGa)As. Photolithography can be successfully used, and we have proved it to be desirable, especially for high concentraction cells that require close-spaced finger patterns with thick contacts to provide minimum series resistance in high current operation at over 500 suns. However, the process has several problems for high efficiency cells:

- The photolithographic technique requires two separate photoresist steps involving the use of alkaline solutions. They generally cause some surface deterioration and oxide formation.
- 2) With thin layers less than 0.5 μm, surface deterioration and oxide formation can cause problems. It seems also that the reactivity of the epitaxial layer increases as the junction gets closer to the top surface, possibly because of the increased strain at the junction, affecting the surface reactivity.
- 3) The oxide provides a good AR coating on the surface of the cells that is optimum for an interface to air. However, the refractive index (~1.8) is not very good for a glass cover. The removal of the oxide by sputtering is touchy for thin layers and often causes additional damage.
- 4) The economics of setting up a complete line of photolithographic processing for high efficiency cells is not attractive until the volume of cells goes above several hundred thousand per year.

It is noteworthy that the silicon cells are presently being made using mechanical masks. Since compatibility with silicon cell technology is a definite advantage in rapid transition to large scale production, it would appear advantageous to proceed with the mechanical mask approach where it is practicable. We have demonstrated that the mechanical mask approach is fully acceptable. We are also, however, capable of utilizing the photolithographic process and are, indeed, developing it for the terrestrial concentrator cell on another program. We believe that with this parallel development, we will be fully capable of using either technique.

## **Contact Annealing Studies**

In studying the performance of the cells with shallow junctions, we noticed that an increasing number of them displayed leaky I-V characteristics. An investigation of the processing history of these cells suggested that the problem was due at least in part to the annealing of the contacts. We therefore conducted a series of experiments to determine the influence of annealing on contact performance.

Typical curves showing the effect of annealing temperatures and times on solar cell performance are shown in Figures 16 and 17. Cell 1817 was first annealed at 425°C (3 minutes) and subsequently annealed at 450°C (3 minutes). After annealing at 450°C, the cell became very leaky. The cell was then cleaved and divided into four equal areas. Figure 18 shows the dark I-V characteristics of two such areas. The second quarter shows leaky I-V characteristics. (It is even possible that an annealing temperature of 425°C is too high for this cell.) A further example, using a new cell (1833), of the effect of contact annealing temperature on cell performance is given in Table 9. The efficiencies given in the last column are for the bare cells without AR coating or glass cover and would correspond to over 15 percent AMO for the completed cell. We proceeded to study the problem in two stages: 1) the reduction of the cell open circuit voltage and 2) the origin of the problem and its geographic location in the cell.

- The lowering of V<sub>OC</sub> can be explained by the increasing diode leakage current caused by the impurity diffusion to the junction. The impurity may be Au or Zn. The increased leakage current is measured by the dark I-V characteristics at each sintered stage.
- 2) To investigate whether this impurity diffusion occurs only locally, the same cell (No. 1822) was cleaved and divided into three regions. The photo I-V characteristics are measured for each region as shown in Figure 19. Both region 1 and region 2 have  $V_{\rm OC}$  about 1 volt, and region 3 has  $V_{\rm OC}$  0.9 volt. Thus, it can be seen that the degradation of cell performance is only caused by regional defects.

TABLE 9. EFFECT OF ANNEALING ON CELL PERFORMANCE

		Cell 1833	3		
		D = 0.4	μm		
		$x_{j} = 0.3$	μm		
V 1 79	tree gits		Photo I-V C	haracteristics	
Annealing Temperature, OC	Annealing Time, min, sec	I <sub>sc,</sub> mA	V <sub>oc,</sub>	FF	η,%
375	1, 49	84	0.98	0.71	10.7
425	2, 18	83	0.97	0.74	11.0
450	3, 29	85	0.89	0.78	11.0

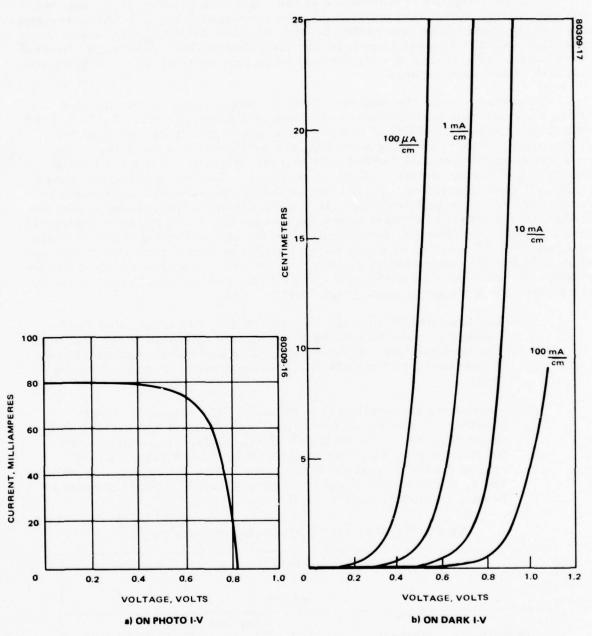


FIGURE 16. 425°C ANNEALING TEMPERATURE EFFECTS (CELL 1817)

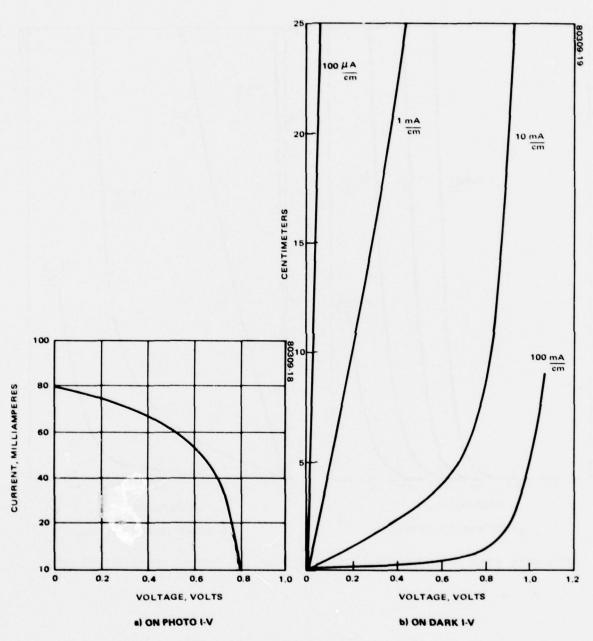


FIGURE 17. 450°C ANNEALING TEMPERATURE EFFECTS (CELL 1817)

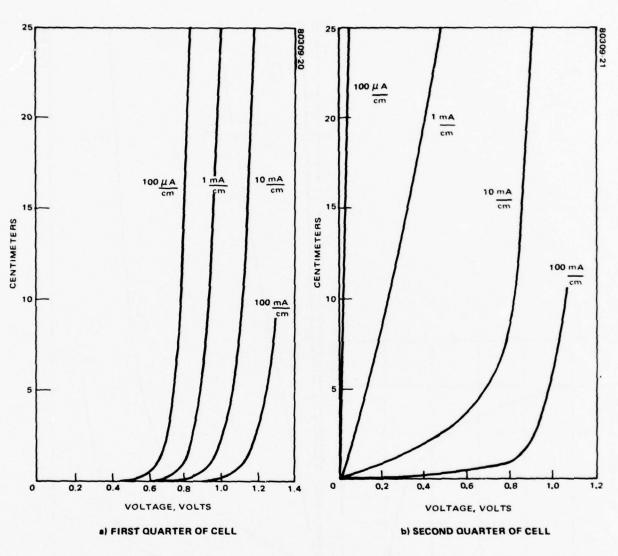


FIGURE 18. DARK I-V CHARACTERISTICS FOR CLEAVED AND DIVIDED AREAS OF CELL 1817

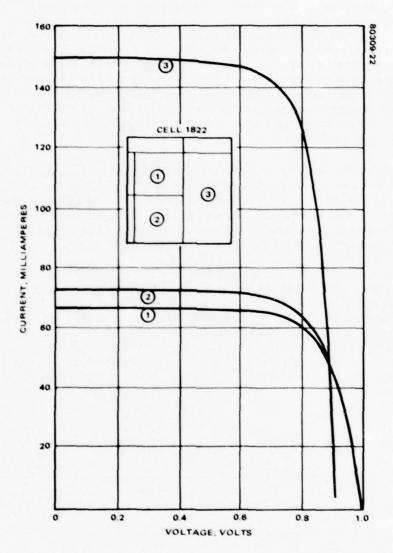


FIGURE 19. CELL 1822 PHOTO I-V CHARACTERISTICS

These results indicate that there is some migration of either Au or Zn in localized areas in the cell that causes serious degradation of cell performance. This condition is aggravated when the junction depth from the contact becomes smaller than a micron. We believe that dislocations produced in the strained region close to the heterophase boundary may contribute to this problem. The larger the cell area, the greater the probability of such a problem occurring locally. It is also interesting to note that the problem is aggravated when the Al concentration goes higher, since the strain at the interface is larger. We believe, however, that once the problem and its causes are understood, processing methods can alleviate and ultimately eliminate the problem. We investigated the cell processing steps in close detail using the new (AlGa)As solution to establish the optimum conditions. Since thinner window layers and shallower junctions are necessary for obtaining maximum efficiency and low radiation damage, these studies were especially significant.

Since high Be doping would cause additional problems in the window layer, we proceeded to study the behavior of contacts to the (AlGa)As layer as a function of Be doping. These experiments showed that some cells with low open circuit voltages ( $V_{\rm OC}$ ) had unusually low Be concentrations. The junction depth measurements on these cells showed that they had unusually shallow junctions of ~0.2  $\mu$ m or lower (Table 10).

We noticed on cells fabricated under these conditions that lower annealing temperatures (<420°C) for contacts could lead to improved open circuit voltages. This is, however, an unacceptable procedure. With junctions deeper than ~0.25  $\mu m$ , we have almost never seen such behavior. Even cells grown with only ~0.18  $\mu m$  junction depth sometimes show normal behavior, which strongly suggests that the problem with shallow junctions is caused by local variations in the junction region which tend to affect the performance of the large area cells. Careful process refinement should resolve these problems.

TABLE 10. GaAs CELLS WITH VERY SHALLOW JUNCTIONS

Cell No.	Window Layer Thickness, µm	Junction Depth, µm	Open Circuit Voltage, V
1945	0.3	0.18	0.85
1946	0.3	0.18	0.9
1956	0.35	0.18	1.0
1936	0.30	0.25	0.99
1848	0.50	0.30	0.89
1849	0.50	0.30	0.94

A prime suspect in the anomalous behavior in shallow junction, thin window layer cells is the gold in the An-Zn contact, which is known to be a fast diffuser, especially along strain boundaries in GaAs. This conclusion is strengthened by the fact that varying Zn by a factor of 2 does not produce any change in Au-Zn contact behavior. Since Au is known to cause problems in the Au-Ge-Ni contacts commonly used in microwave devices, we feel that elimination of Au from the contacts is desirable. Ag-Zn as a contact is being presently investigated on the HESP program. The behavior of Ag-Zn in high Al(AlGa)As is being examined in detail with shallow junctions and thin window layers.

#### 3. CONCLUSIONS

The LPE layer growth is well in hand, and the HRL infinite solution technique has been proven satisfactory for growing the solar cell structures needed. Additional refinement in growth temperatures and cooling rates should further improve the heterojunction region and reduce the strain fields associated with it. A more careful study of dopant concentrations at the electrical junction and of the possible advantages of alternative p-type dopants such as Mg may improve the junction and remove some of the limitations noted with Be. The cells made according to the present process are, however, suitable for space experiments to establish GaAs ceil acceptability.

(AlGa)As contact technology is a difficult problem at best. We have produced Au-Zn contacts that are acceptable for most normal operations. With improved annealing procedures and careful control of the temperature during the sputtering operation, the contacts are mechanically and electrically reproducible. The Au-Zn contact, however, has some limitations because of the tendency of Au to migrate unpredictably through strain boundaries in the window layer. Further, the contact is only stable below 400°C. The addition of a refractory metal to the alloy would appear to be a solution. Ti, Ta, Cr, and Ni are good candidates. Application of a thin film of one of these materials to the surface prior to contacting should be tried. We would prefer to attempt this step using Ag-Zn rather than Au-Zn in order to eliminate Au from the contacts. Such a contacting study would involve a systematic and sustained investigation of several month's duration. Contacting directly to (AIGa)As is, however, a prerequisite of reducing the complexity of cell fabrication if a thin window and a shallow junction are to be successfully included in the cell structure. HRL is presently pursuing this technology under an Independent Research and Development (IR &D) project.

#### SECTION V

#### SOLAR CELL CHARACTERIZATION AND PERFORMANCE

#### 1. CARRIER CONCENTRATION IN LAYERS

The carrier concentration for the n GaAs buffer layer and for the p diffused GaAs layer was obtained from Hall effect measurements. The carrier concentration of the p diffused layer was found to be close to that of the (AlGa)As layer. We formed a thick layer (3  $\mu m$ ) by the diffusion of beryllium (Be) from the (AlGa)As layer into the epitaxially grown n layer. Two samples were made for Hall effect measurements. The (AlGa)As layer on one sample was etched off completely, and the Hall measurement was made on the p diffused layer. On the other sample, the measurement was made directly on the(AlGa)As layer. The carrier concentration in both layers is of the same order. The Hall measurement results are given in Table 11.

Both the secondary ion mass spectroscopy (SIMS) and Hall measurements indicate a higher p type doping level in the GaAs than in the (AlGa)As. The exact reason for this is not clear. It could be a difference in the impurity level position in the band gaps of the two materials, with the Be level in GaAs being shallower. This aspect needs to be studied in greater detail by taking Hall measurements as a function of temperature.

## 2. DIFFUSION LENGTH MEASUREMENTS

Figure 20 shows the electron beam induced current (EBIC) technique developed under a separate program at HRL to measure the diffusion lengths

TABLE 11. HALL EFFECT MEASUREMENT RESULTS

Layer	Thickness, µm	μ <sub>p</sub> ,V-sec	N <sub>A</sub> , cm <sup>-3</sup>
(A1Ga)As	3.7	114.2	1.5 × 10 <sup>18</sup>
Diffused p layer	3.0	93.2	2 x 1018

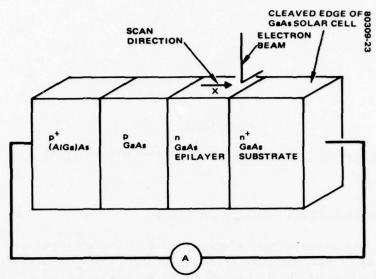


FIGURE 20. EBIC METHOD OF MINORITY CARRIER DIFFUSION LENGTH MEASUREMENT USING SEM TECHNIQUE

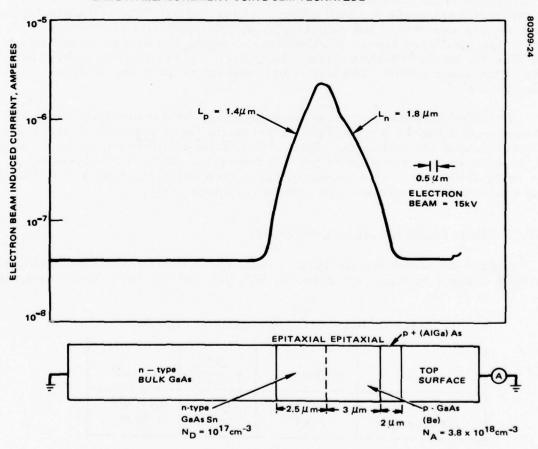


FIGURE 21. SEM MINORITY CARRIER DIFFUSION LENGTH MEASUREMENTS GaAs-GaAs-(AIGa)As SOLAR CELL

# TABLE 12. DIFFUSION LENGTHS MEASURED IN EACH LAYER OF (AIGa) As-GaÅs SOLAR CELL

Material	Doping Density, cm <sup>-3</sup>	L <sub>n</sub> , μm	L <sub>p</sub> , μm
(AlGa)As	2.0 × 10 <sup>18</sup>	0.75	
GaAs (p) EPI	$1.5 \times 10^{18}$	1.8	
GaAs (n) EPI	1 x 10 <sup>17</sup>		1.4
GaAs substrate	$7 \times 10^{17}$		0.6

in (AiGa)As-GaAs solar cells. In this technique, the beam of a scanning electron microscope (SEM) generates minority carriersnear the surface of the semiconductor which diffuse toward the junction. The induced junction current I varies exponentially with scan distance X.

$$I(x) = I_o \exp \left(-\frac{X}{L}\right)$$

In one of our first successful measurements, the doping density for the n substrate and n buffer layer was  $7 \times 10^{17}$  cm<sup>-3</sup> and  $1 \times 10^{17}$  cm<sup>-3</sup>, respectively. The diffused p layer (NA=3.8 ×  $10^{18}$  cm<sup>-3</sup>) forming a junction within the n buffer layer measured 3  $\mu$ m thick, and the (A1Ga)As window layer (NA=2.5 ×  $10^{18}$  cm<sup>-3</sup>) was 2  $\mu$ m thick. Figure 21 shows the logarithmic plot of the induced current versus scan distance along the cleaved surface for this measurement. The minority carrier diffusion length in each layer was determined from the linear portion of the log I versus X plot. The results are summarized in Table 12. However, only a small number of samples was tested. The diffusion length in each layer still needs to be confirmed by a larger number of measurements.

## 3. JUNCTION DEPTH MEASUREMENTS

Junction depth is an important parameter for (AlGa)As-GaAs solar cells because of the large optical absorption coefficient in GaAs. The correlation between junction depth, minority carrier diffusion length, and solar cell efficiency would require us to keep the junction shallow (see Section II, Theoretical Model). We use three different techniques to measure junction depths in our solar cell structures. These are identified in Table 13. Optical examination of the cleaved edge is not satisfactory for measuring junction thickness less than 0.5  $\mu m$  because this thickness is of the same order as the wavelength of the light used. The beveled structure seems to display the various layers fairly well if the polishing can be done carefully.

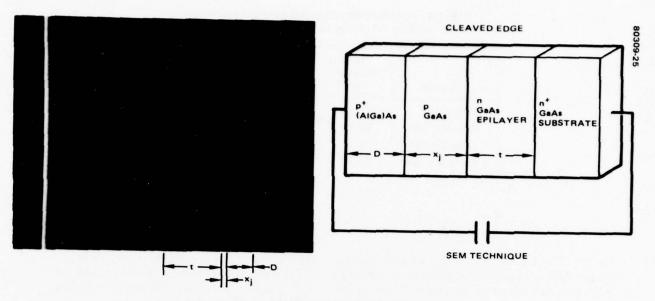


FIGURE 22. JUNCTION DEPTH DETERMINATION

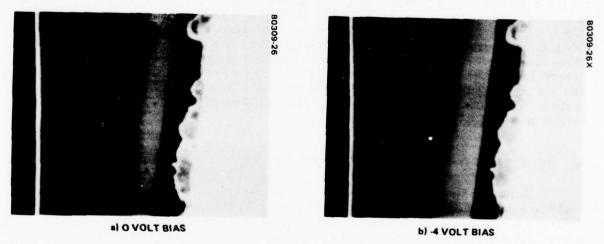


FIGURE 23. SEM PHOTOS OF (AIGa)As-GaAs SOLAR CELL 283 (MAGNIFICATION 10200X)

TABLE 13. TECHNIQUES USED FOR JUNCTION DEPTH MEASUREMENTS

Technique	Sample Structure	Remarks
SEM	Cleaved mesa diode	
SIMS	(AlGa)As-GaAs	Slow etching rate required costly machine time
Staining and optical	Cleaved	Measurable distance >1 λ
microscope	Beveled	Careful polishing needed; reliable results with optimum etch

The scanning electron microscope technique with voltage contrast mode allows us to determine junction depth with sufficient reliability. The arrangement used is shown in Figure 22. Typical SEM patterns observed are shown in Figure 23 for 0 and -4 volt bias. The bias improves the contrast and makes measurements easier. These photos show that the reverse bias actually widens the depletion width. The depletion width increase agrees well with the calculation based on the abrupt junction theory (see subsection II. 1, Equation 10). The doping density used in this calculation again confirms the Hall effect measurement.

The result obtained by SEM was also confirmed by measurements using SIMS. A typical result from SIMS measurements is shown in Figure 24. The initial 0.5  $\mu$ m is the (A1Ga)As layer where the concentration of A1 and As is relatively high. The p diffused layer starts where the A1 concentration is being reduced and ends at the junction where Be concentration has vanished. This layer is approximately 1  $\mu$ m thick. This measurement also shows that the diffused p layer is uniformly doped with Be. Of these techniques, the SEM seems to be the best and most convenient tool to determine the junction depth.

## 4. JUNCTION DEPTH MEASUREMENT VERSUS GROWTH PARAMETERS

Table 14 shows the junction depth as a function of growth parameters. The variation of junction depth as a function of growth time is shown at the top of the table, its variation as a function of diffusion time following 5 minutes of growth is shown in the middle, and junction depth at higher growth temperatures is shown at the bottom. The results, summarized in Figure 25, lead to the following conclusions:

- 1) Shallow junction (less than 0.5  $\mu$ m) can be obtained below 810  $^{\circ}$ C if growth times are held to less than 5 minutes.
- The diffusion time at 810°C following 5 minutes growth time does not appreciably increase junction depth.
- 3) The junction depth, x, increases at higher growth temperature.

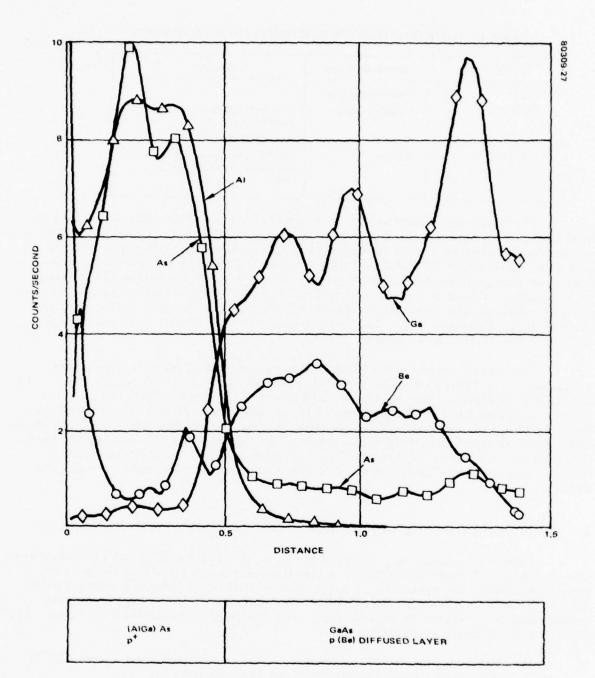


FIGURE 24. SIMS MEASUREMENTS ON (AIGa)As-GaAs SOLAR CELL

TABLE 14. JUNCTION DEPTH MEASUREMENTS VERSUS GROWTH PARAMETERS

Cell No.	Initial Growth Temperature, $T_g$ , $^{\circ}C$	$\Delta T_{f g}$	Growth Time, t <sub>g</sub> , min*	Cooling Rate, ΔTg/tg, <sup>O</sup> C/min	Be Concentration, cm <sup>-3</sup>	Junction Depth, x <sub>j</sub> , μm	(AlGa)As Layer Thickness D, μm
	Jun	ction De	pth Variatio	n as Function of	Growth Time		
721	809.7	0.8	3+0	0.267	1 x 10 <sup>18</sup>	0.42	0.25
727(a)	810.0	1.05	4+0	0.262	1 x 10 <sup>18</sup>	0.46	0.67
730(c)	810.0	1.3	5+0	0.26	1 x 10 <sup>18</sup>	0.54	
727(b)	810	3.4	10+0	0.34	1 x 10 <sup>18</sup>	0.75	2.59
727(c)	822	5.3	20 + 0	0.265	1 x 10 <sup>18</sup>	1.15	6.30
	June	tion Dep	oth Variation	as Function of D	oiffusion Time		
751	809.7	1.25	5+5	0.25	1 x 10 <sup>18</sup>	0.55	1.12
740	809.7	1.1	5 + 10	0.22	1 x 10 <sup>18</sup>	0.60	1.30
738	809.9	1.45	5 + 15	0.29	1 x 10 <sup>18</sup>	0.65	1.20
737	810	1.25	5 + 2	0.25	1 x 10 <sup>18</sup>	0.66	1.42
		Junction	Depth at H	igher Growth Ten	peratures		
768	822	2.5	10+0	0.25	1 x 10 <sup>18</sup>	1.15	5.48
727	822		20+0	0.16	1 x 10 <sup>18</sup>	1.15	
761	822	0.80	5+10	0.16	1 x 10 <sup>18</sup>	0.90	2.0
756	822	1.25	5+5	0.25	1 x 10 <sup>18</sup>	1.0	2.5
782	836	0.64	4 + 10	0.16	1 x 10 <sup>18</sup>	0.87	1.34
791	836	0.80	5 + 10	0.16	1 x 10 <sup>18</sup>	1.00	0.62
792	836	1.28	8 + 10	0.16	1 x 10 <sup>18</sup>	1.20	2.33
526	836		10 + 20	0.05	3 x 10 <sup>18</sup>	2.00	1.0

<sup>\*</sup>Growth time + diffusion time.

4) The junction depth x; increases at a faster rate at the beginning of the growth. This probably reflects the increased influence of the solution with its higher Be concentration as a diffusion source at the inception of epitaxial growth. The effect of the solution on initial stages of growth has to be coupled with the relative positions of the energy level of Be in the band gaps of GaAs and (AlGa)As to explain fully the behavior of Be as a dopant in the GaAs solar cell structure.

These findings were incorporated into a modified process for the growth of LPE layers to yield solar cells with improved radiation resistance (see Section IV). Table 15 gives the results for these cells.

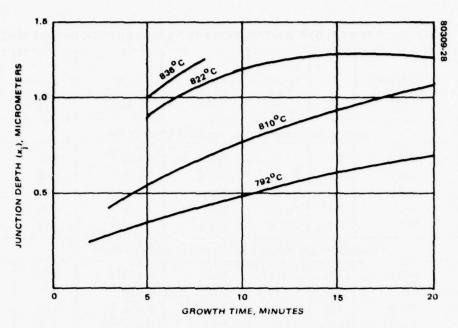


FIGURE 25. JUNCTION DEPTH (xi) VERSUS GROWTH TIME

TABLE 15. JUNCTION DEPTH MEASUREMENTS VERSUS GROWTH TIME FOR RADIATION RESISTANT CELLS

Cell No.	Initial Growth Temperature, T <sub>g</sub> ,	ΔTg	Growth Time, t <sub>g</sub> , min*	Cooling Rate, ^Tg/tg, °C/min	Be Concentration, cm	Junction Depth, x <sub>j</sub> , μm	(AlGa)As Layer Thickness, D, μm
2099	792	0.4	2	0.25	1 x 10 <sup>18</sup>	0.25	0.4
LEPI 1103	792	2.8	5	0.56	1 x 10 <sup>18</sup>	0.3	_
LEPI 1102	792	17.8	20	0.89	1 x 10 <sup>18</sup>	0.7	4.5

## 5. DARK I-V CHARACTERISTICS

Dark current-voltage (I-V) characteristics are an important measure of solar cell performance because they reflect the cell's fill factor and open circuit voltage. Dark I-V characteristics are determined by the combined effect of the current transport mechanisms, mainly diffusion and recombination currents.

The diffusion current-voltage relationship for forward bias was expressed in Equation 16 (Section II) as

$$I_{diff} = I_{ol} (e^{qV/kT} - 1)$$

where V is the voltage drop across the junction and I is the leakage current density shown in Equation 17, i.e.,

$$I_{ol} = qn_{i}^{2} \left( \frac{D_{n}}{N_{A}L_{n}} \frac{S_{p} \cosh \frac{D+x_{j}+w}{L_{n}} + \frac{D_{n}}{L_{n}} \sinh \frac{D+x_{j}+w}{L_{n}}}{\frac{D_{n}}{L_{n}} \cosh \frac{D+x_{j}+w}{L_{n}} + S_{p} \sinh \frac{D+x_{j}+w}{L_{n}}} \right) + qn_{i}^{2} \left( \frac{D_{p}}{N_{D}L_{p}} \frac{S_{n} \cosh \frac{t}{L_{p}} + \frac{D_{p}}{L_{p}} \sinh \frac{t}{L_{p}}}{\frac{D_{p}}{L_{p}} \cosh \frac{t}{L_{p}} + S_{n} \sinh \frac{t}{L_{p}}} \right)$$

The generation and recombination current-voltage relationship under forward bias condition is

$$I_{gr} = I_{o2} \begin{pmatrix} \frac{qV}{2^{kT}} \\ e & -1 \end{pmatrix}^{*}$$
(28)

where

$$I_{02} = \frac{qn_i^w}{\sqrt{\tau_{\eta_0}\tau_{\rho_0}}}$$

<sup>\*</sup>Equation 18 (Section II) is an expanded expression of this value.

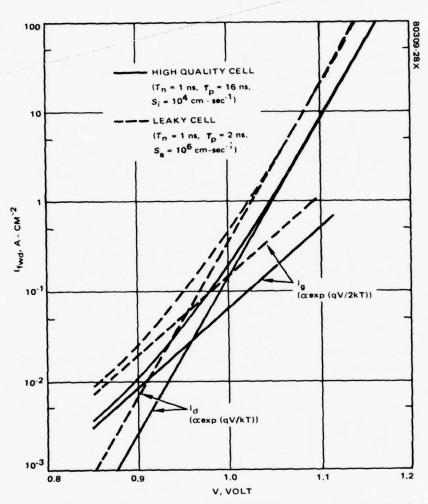


FIGURE 26. THEORETICAL DARK I-V CURVES FOR GaAs SOLAR CELLS

Thus, the total forward current-voltage relationship is given by the sum of these two current components, namely,

$$I = I_{o1} \begin{pmatrix} \frac{qV}{kT} \\ e & -1 \end{pmatrix} + I_{o2} \begin{pmatrix} \frac{qV}{2kT} \\ e & -1 \end{pmatrix}$$
(29)

Figure 26 shows the theoretical dark I-V relationship for a high quality GaAs cell (solid line) and for a leaky GaAs cell (dashed line). The maximum power point normally occurs in a region where both current contributions are important. However, for a leaky cell with excess dark current, the generation-recombination current will be the dominant contributor at the maximum power point.

Figure 27a shows a typical I-V measurement of our high quality (AlGa)As-GaAs cell. It has two exponential regions with slopes qV/2.1~kT (n = 2.1) and qV/1.8~kT (n = 1.8), respectively. The decreasing slope of the current around 0.1 ampere results from the series resistance of the device (around 0.1 ohm). At the short circuit current value of 120 mA, 12 mV are lost across this resistance. Figure 27b shows the I-V characteristics for a leaky GaAs cell. The slope of log I-V is qV/2.1~kT (n = 2.1) at the maximum power point. Thus, for these cells, it is seen once again that the I-V characteristics are generation-recombination limited.

The lateral uniformity of the p-n junction between the p diffused layer and n grown layer was examined with a scanning electron microscope operated in the electron beam induced current (EBIC) mode. Figure 28 shows an EBIC picture of a cross section of an (AlGa)As-GaAs mesa structure. Figure 29 is the scanning electron micrograph obtained in the EBIC mode for the same sample. The presence of a laterally continuous junction is indicated by the uniform collection of induced current in the space charge region. This technique can be used to examine the junction quality of the entire area (2 x 2 cm) of the solar cell.

# 6. ELECTROLUMINESCENCE EXPERIMENT

A light emission image in the forward biased  $2 \times 2 \text{ cm}$  (AlGa)As-GaAs solar cells is shown in Figure 30. The photo shows nonradiative dark spots. Three different efficiency solar cells are used for comparison. The cell with the largest density of nonradiative dark spots has the lowest efficiency.

In the case of reverse bias, emission spots originally from the microplasma were observed. Figure 31 shows the reverse biased image of the diode through the infrared microscope; Figure 32 shows the comparable image produced by the optical microscope (visible range). Sometimes the

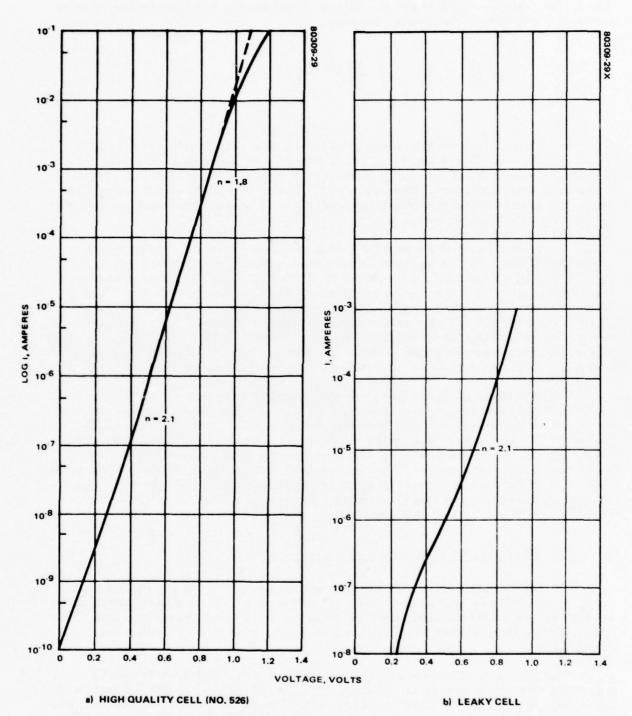


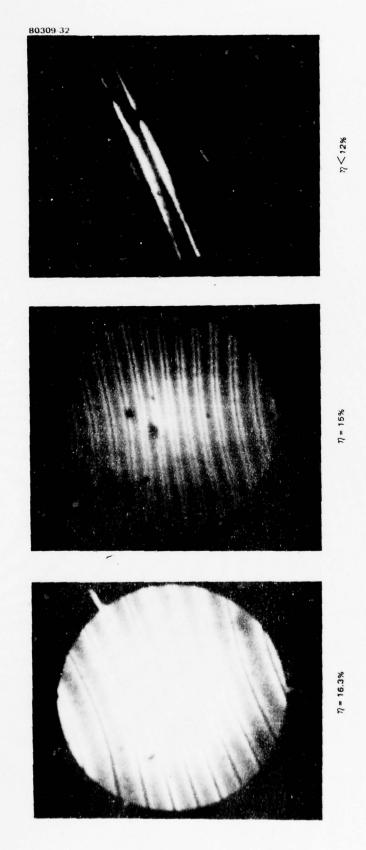
FIGURE 27. (AIGa) As-GaAs DARK I-V CHARACTERISTICS



FIGURE 28. EBIC PHOTO OF CROSS SECTION OF (AIGa)As-GaAs MESA STRUCTURE IN BRIGHTNESS CONTRAST MODE



FIGURE 29. SCANNING ELECTRON MICROGRAPH OBTAINED IN EBIC MODE OF SAME SAMPLE SHOWN IN FIGURE 28



SOLAR CELL EFFICIENCIES,  $\eta$  FORWARD BIAS CURRENT, 1.5 A

INJECTION IR LUMINESCENCE DEFECT ANALYSIS (AIGa)As-GaAs SOLAR CELL FIGURE 30.



a) FORWARD BIAS



b) REVERSE BIAS

FIGURE 31. EMISSION SPOTS ORIGINATING FROM DEFECTS — ELECTROLUMINESCENCE EXPERIMENT ON (AIGa) As GaAs SOLAR CELL 433 USING INFRARED MICROSCOPE

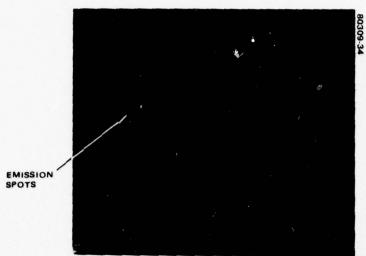
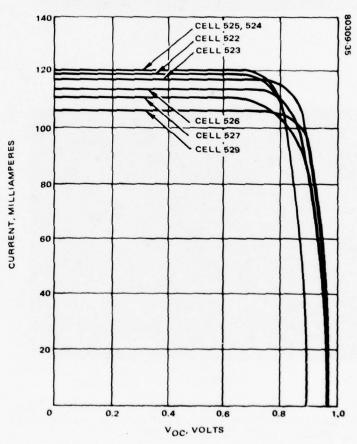


FIGURE 32. EMISSION SPOTS ORIGINATING FROM DEFECTS - REVERSE BLASED IMAGE OF (AIGa) As-GaAs SOLAR CELL IN OPTICAL MICROSCOPE



CONSECUTIVE CELLS GROWN BY HUGHES LPE FIGURE 33. (AIGa)As-GaAs SOLAR CELL PHOTO I-V

microplasma emissions appear at positions where the nonradiative dark spots would be, and these emission spots occur at different reverse bias voltages. This shows that the breakdown voltages at some of these positions are higher than those at other positions. It is reasonable to assume that two different types of defects give rise to the spots observed in the two regions of the spectrum examined by the infrared and optical microscopes.

## 7. (AlGa)As-GaAs SOLAR CELL PERFORMANCE

Table 16 shows the performance of selected (AlGa)As-GaAs solar cells. Observations include the following:

- 1) Dependence of  $V_{OC}$  on n buffer layer (ND) carrier concentration
- 2) Comparatively low sensitivity of  $I_{sc}$  to the buffer layer carrier concentration in the range of  $4 \times 10^{15}$  to  $3 \times 10^{16}$  cm<sup>-3</sup>
- 3) Influence of (A1Ga)As layer thickness, D, on I sc

Figure 33 shows the current-voltage relationships (I-V) of these cells. Figure 34 shows the spectral response of cell 526. The numbers in the diagram give the normalized quantum efficiency for photon to electron conversion as measured on a 2 x 2 cm GaAs cell using light of 0.6  $\mu$ m wavelength. The measurement is approximately 5 percent.

The excellent uniformity of response is indicative of the quality of the epitaxial layer. Measurements at other wavelengths confirm the same uniformity at all parts of the solar spectrum between 0.4 and 0.9  $\mu$ m.

TABLE 16. HRL GaAs SOLAR CELL CHARACTERISTICS (JANUARY 1977)

Cell No.	N <sub>D</sub> X 10 <sup>17</sup> cm <sup>-3</sup>	D, μm	I <sub>sc'</sub> mA	Voc. mV	η (AM0)	FF
522	0.04	0.4	115	900	15.9	0.83
524	0.04	0.4	116	900	16.2	0.83
525	0.04	0.4	116	900	15.9	0.82
523	0.3	0.4	118	980	17.5	0.82
526	0.3	1	110	980	17.2	0.86
527	0.3	1	109	980	16.9	0.85
529	0.3	2	106	980	16.1	0.82

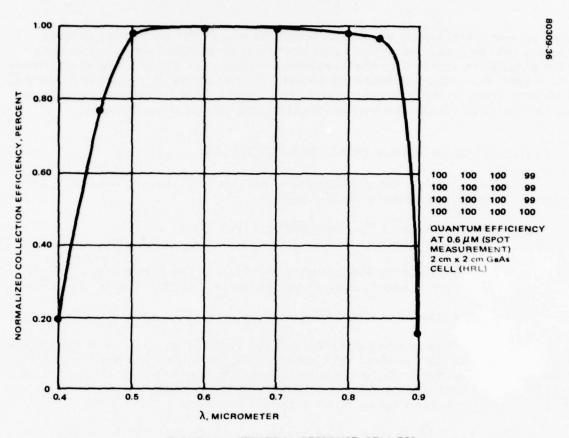


FIGURE 34. SPECTRAL RESPONSE, CELL 526

For comparison of theory and experiment the measured values of  $I_{sc}$  from Table 16 are shown with the theoretical curves of Figure 35. Figure 35 plots the measured and theoretical values of  $I_{sc}$  as a function of (AlGa)As layer thickness. The parameters used in this calculation are  $L_p$  = 2 $\mu$ m, W = 0.14  $\mu$ m,  $x_j$  = 0.5  $\mu$ m.

Figure 36 shows the measured open circuit voltage  $V_{\rm OC}$  as a function of base doping densities (ND). Each delta in the plot represents the best measured  $V_{\rm OC}$  values for the 2 x 2 cm² (AlGa)As-GaAs solar cells. For a given doping density there is some variation in  $V_{\rm OC}$  among the cells. This is due to the differences in the diode saturation current. The large saturation current will lower the  $V_{\rm OC}$ . The continuous line in Figure 36 represents the  $V_{\rm OC}$  calculated for n = 1 as a limiting case. Again, the higher doping density reduces the diode saturation density  $I_{\rm OC}$ , resulting in high  $V_{\rm OC}$ .

The fill factors for these relatively deep junction (>1  $\mu$ m) cells, shown in Table 16, are excellent; their maximum value of 0.86 is close to the theoretical value of 0.88.

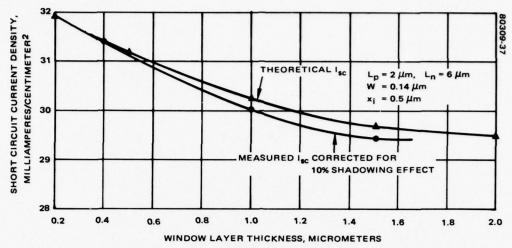


FIGURE 35. SHORT CIRCUIT CURRENT DENSITY VERSUS (AIGa)As LAYER THICKNESS

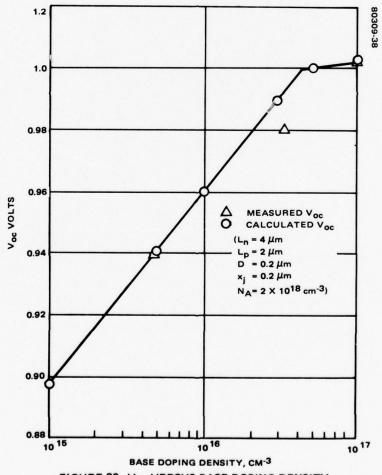


FIGURE 36.  $V_{\rm oc}$  VERSUS BASE DOPING DENSITY

### SECTION VI

### RADIATION RESISTANCE STUDIES

### 1. INTRODUCTION

During the last 2 years, Hughes has done a considerable amount of work on understanding the effects of electron radiation damage and proton radiation damage. This work was accomplished with program funding supplemented by IR&D funds and contracts from NASA (NAS1-14727) and the Air Force (High Efficiency Solar Panel). The results of this work are presented here in summary form.

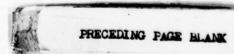
### 2. STUDY SUMMARY

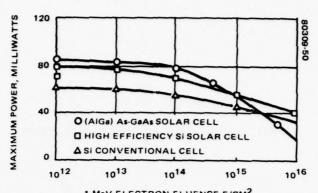
The behavior of solar cells under radiation environment is of great importance for space application. Previous studies have shown (AlGa)As-GaAs solar cells to achieve an efficiency of 18.5 percent AM0<sup>14</sup> with a radiation resistance equal to or better than that observed in violet silicon cells. <sup>18</sup> We report here the radiation effect on large-area (2 x 2 cm) (AlGa)As-GaAs solar cells fabricated at HRL using the infinite melt liquid phase epitaxial (LPE) growth system.

GaAs has a large optical absorption constant and a short diffusion length; essentially, all the photovoltaic response is close to the GaAs surface. The radiation damage beyond this active region has a negligible effect on cell performance. Consequently, the reduction in the required minority carrier diffusion length and the relative shallowness of the active region are the key factors that can be exploited to make GaAs solar cells more radiation resistant. Data consistent with these observations is presented below.

### Experimental

The Dynamitron particle accelerator at JPL was used as the electron source for high-energy electron irradiation; the irradiations were performed in vacuum at room temperature. The uniformity over the test plane was ±4 percent with no areas of discontinuity. Fluxes and fluences were measured with a Faraday cup the current of which was integrated to establish electron fluences and to automatically stop the irradiation at the desired fluence levels.





1 MeV ELECTRON FLUENCE, E/CM<sup>2</sup>
FIGURE 37. MAXIMUM POWER AS FUNCTION OF 1 MeV

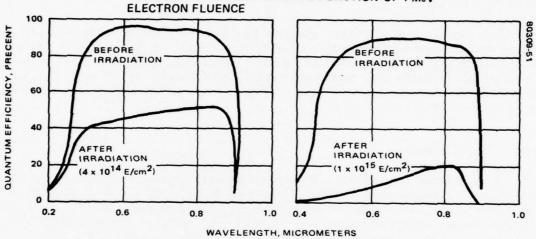


FIGURE 38. (AIGa) As-GaAs SOLAR CELL SPECTRAL RESPONSE BEFORE AND AFTER 1 MeV ELECTRON IRRADIATION

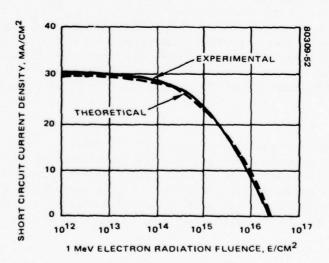


FIGURE 39. SHORT CIRCUIT CURRENT DENSITY VERSUS 1MeV ELECTRON RADIATION FLUENCE

A matrix of the tests performed on the (AlGa)As-GaAs solar cells and on several representative silicon solar cells is given in Table 17.

## Results and Discussion

# Electron Damage

A group of cells was fabricated early in this program for electron radiation tests. These cells were designed to have high efficiency, but no attempt was made to optimize the design parameters to increase radiation hardness. Figure 37 shows the maximum power obtained from the cells plotted against 1 MeV electron radiation fluence. These results were then compared with those for two types of silicon cells, as shown in Table 17. The comparison showed the need to improve these early cells for better resistance to electron radiation damage at fluences in excess of  $4 \times 10^{14} e/cm^2$ .

Figure 38 shows the spectral response before and after electron irradiation. The results show that in these cells the spectral response in the short wavelength region shows greater damage than that in the long wavelength region. Since the optical absorption coefficient is greater for short wavelengths, most of the absorption in this region will be close to the surface of the cell. The photogenerated carriers, therefore, must travel further to reach the junction than do those generated by longer wavelengths. The spectral response of the damaged cells suggested that their junctions had to be relatively deep compared to the minority carrier diffusion length in the damaged layer — a suspicion that was confirmed by the measured junction depth of  $\geq 1 \, \mu m$ . These observations occasioned a more careful examination of the influence of junction depth on radiation damage.

To correlate theory and experiments, Figure 39 shows the (AlGa)As-GaAs solar cell short circuit current density as a function of

TABLE 17. ELECTRON IRRADIATION TEST MATRIX

Electron	Electron Fluence e/cm <sup>2</sup>	Type and Number of Cells						
Energy, MeV		(AlGa)As-GaAs	Si Conventional	Si High Efficiency				
1:0	1 x 1013	3	3	3				
	4 × 1014	3	. 3	3				
	1 x 10 <sup>15</sup>	3	3	3				
	5 × 1015	3	3	3				
	1 x 1016	3	3	3				
0.7	1 x 1015	2						
1.9	1 x 1015	2						

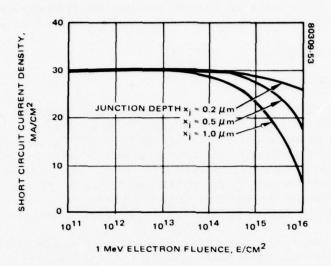


FIGURE 40. PREDICTED (AIGa) As-GaAs SOLAR CELL SHORT CIRCUIT CURRENT DENSITY VERSUS 1 MeV ELECTRON RADIATION FLUENCE

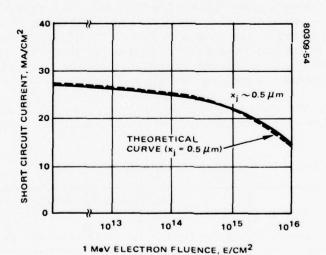


FIGURE 41. SHORT CIRCUIT CURRENT VERSUS ELECTRON FLUENCE LEVEL (1 MeV)

l MeV electron radiation fluence. The continuous curve represents the normalized experimental values. The dotted line is the theoretical curve. Both curves correspond to an (AlGa)As layer thickness of l  $\mu$ m and a junction depth of l  $\mu$ m. For calculating the theoretical curve, the minority carrier diffusion length L was related to the fluence  $\phi$  by the usual relation:

$$\frac{1}{L^2} = \frac{1}{L_0^2} + K_L \phi . {30}$$

The initial diffusion lengths for holes ( $L_{po}$ ) and electrons ( $L_{no}$ ) were assumed to be 2 and 5  $\mu m$ , respectively, in these calculations. The damage constant  $K_L$  for the diffusion length used for both p- and n-type GaAs was deduced by matching the theoretical curve to the experimental curve as shown in Figure 39. It was found to be  $K_L = 7 \times 10^{-8}$ , assuming the same value of  $K_L$  for the n- and p-doped GaAs.

Using this value for  $K_L$ , the short-circuit density was calculated for several junction depths as a function of a 1 MeV electron fluence (Figure 40). Experimental results were in close agreement with these values, showing that radiation damage decreases as junction depth decreases.

On the basis of this analysis we proceeded to fabricate a second generation of (AlGa)As-GaAs solar cells with the goal of decreased sensitivity to the radiation environment. The window layer thickness was made at 0.5  $\mu m$  while the junction depth was decreased to  $\sim\!0.5~\mu m$  by readjusting the LPE layer growth parameters.

Figure 41 shows the measured short circuit current of these shallower junction cells versus 1 MeV electron fluence. The experimentally observed improved radiation resistance is in good agreement with the predictions of the theory. Figure 42 shows the experimental results for both (AlGa)As-GaAs solar cells and newly developed high efficiency Si solar cells as a function of 1 MeV electron irradiation. Also shown for reference are the results for the previous set of irradiated (AlGa)As-GaAs deep junction solar cells.

The spectral responses of the deep junction and shallower junction cells, both before and after irradiation, are given in Figure 43. The figure shows that the radiation damage in the deeper junction cells is concentrated in the short wavelength region, whereas the shallower junction causes the damage to shift to the longer wavelength. This is consistent with our observation that the collection of minority carriers in the p region is not much affected up to the fluence at which the electron diffusion length is reduced to less than the p layer thickness.

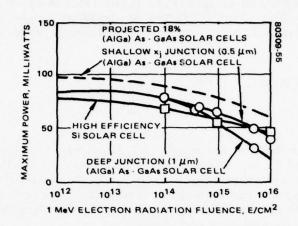


FIGURE 42. MAXIMUM OUTPUT POWER VERSUS 1 MeV ELECTRON FLUENCE

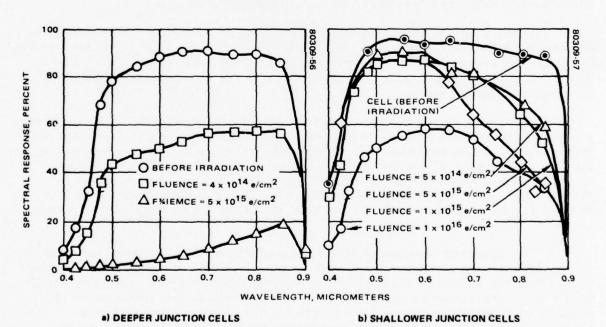


FIGURE 43. (AIGa) As-GaAs SOLAR CELL SPECTRAL RESPONSE VERSUS 1 MeV ELECTRON RADIATION

Figure 44 shows the spectral response of the shallower junction solar cells irradiated at fluences 1 x  $10^{15}$  e/cm² with electron energies varying from 0.7 to 1.9 MeV. As expected at higher energies, these cells show more degradation, probably because  $K_L$  increases with increasing electron energy. Figure 45 shows typical dark I-V characteristics before and after electron irradiation. Although solar cells become more leaky after irradiation, the basic transport mechanism remains the same (as shown by the I-V curves, which remain parallel to each other). This increased leakage current probably results from an increase in the number of recombination centers at the junction.

## Radiation Annealing Studies

GaAs solar cells damaged by radiation recover their efficiency when annealed at low temperatures on the order of  $200^{\circ}\text{C}$  to  $300^{\circ}\text{C}$ . 19.20 Some preliminary thermal annealing experiments on the radiation-damaged (AlGa)As-GaAs solar cells were performed in the HRL laboratory. The cells were irradiated at fluences of 1 x  $10^{15}$  e/cm<sup>2</sup> with electron energies varying from 0.7 MeV through 1.0 MeV to 1.9 MeV. Subsequently, they were annealed in vacuum at temperatures of over  $200^{\circ}\text{C}$ . Figure 46 shows the effect of annealing as a function of annealing time and temperatures.

Figure 47 compares the spectral response of these cells after the annealing step with the spectral response before and after electron irradiation. The long wavelength region shows significant recovery. This suggests that the annealing leads to a significant recovery in the minority carrier diffusion length in GaAs after radiation damage.

Figure 48 shows the dark I-V characteristics of these cells. These cells show leaky p-n junctions after irradiation; however, they almost completely recover to their pre-irradiation condition after annealing at 210°C. These results indicate that (AlGa)As-GaAs solar cells can be annealed at practical temperatures to remove radiation damage, a fact that could be exploited for longer space missions.

### Conclusion

The Hughes studies clearly demonstrate that, in addition to having a higher absolute efficiency than silicon cells, GaAs cells also have superior radiation resistance—a superiority that results in less performance degradation from beginning of life to end of life. The studies also show that the liquid phase epitaxial growth method can be successfully used to grow large area epitaxial layers suitable for fabricating solar cells with reproducible parameters necessary for further refinements that could yield AM0 efficiences in excess of 18 percent beginning of life. Reduction of junction depth to ~0.2 to 0.3  $\mu m$  should lead to further reduction in radiation damage.

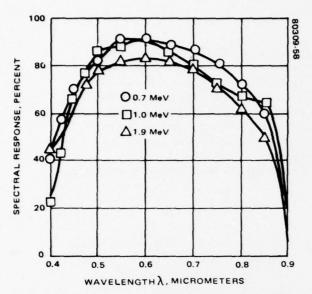


FIGURE 44. SHALLOW JUNCTION CELL SPECTRAL RESPONSE FOR SEVERAL ELECTRON ENERGIES

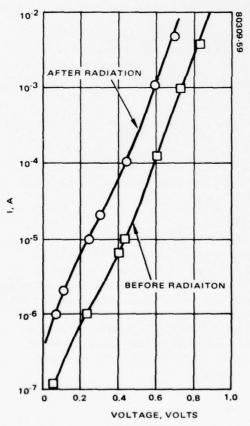


FIGURE 45. DARK I-V CHARACTERISTICS BEFORE AND AFTER ELECTRON IRRADIATION

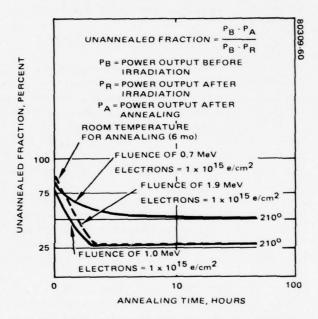
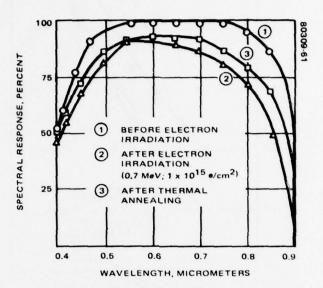
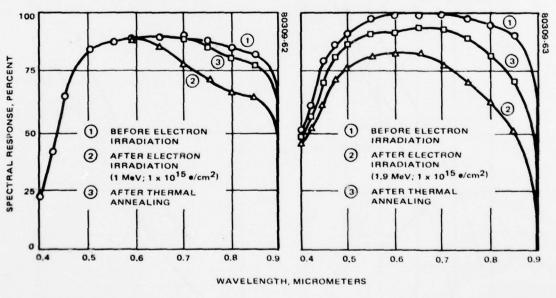


FIGURE 46. UNANNEALED FRACTION VERSUS ANNEALING TIME

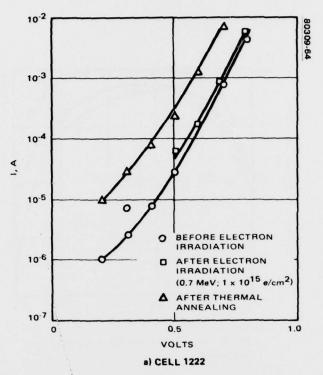


a) BEFORE AND AFTER THERMAL ANNEALING— CELL 1222



b) BEFORE AND AFTER THERMAL ANNEALING-CELL 1008 c) BEFORE AND AFTER IRRADIATION AND AFTER THERMAL ANNEALING — CELL 1278

FIGURE 47. (AIGa) As-GaAs SOLAR CELL SPECTRAL RESPONSE



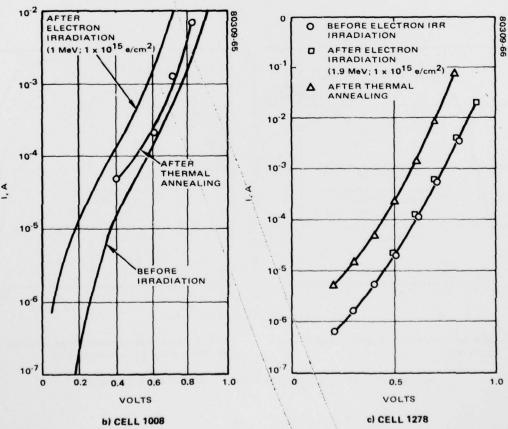


FIGURE 48. DARK I-V CHARACTERISTICS BEFORE AND AFTER THERMAL ANNEALING

#### SECTION VII

## THERMAL CYCLING, HUMIDITY, AND TAPE PEEL TESTS

#### 1. THERMAL CYCLING TESTS

Five cells were subjected to thermal cycling in conformity with the contractual requirement. The thermal cycles were from -195°C to 110°C with a cooling rate of ~100°C/min such that the entire cycle took place in about 6 minutes. The cells were subjected to 100 cycles while the cell temperature was monitored by a thermocouple. The cells successfully survived the tests, displaying no evident problems in electrical characteristics, as seen from Figure 49, although one cell was slightly damaged during handling.

Independently of these cycling tests, cells were subjected to temperatures up to 250°C for several hours during the thermal annealing of radiation damaged cells conducted at HRL (see Section VI). After up to 20 hours at this temperature, these cells displayed no apparent degradation. Using the same equipment used in the annealing studies, we subjected a number of cells to thermal cycles from -180°C (liquid N2 temperature) to 250°C without causing any degradation to the majority of them. Some cells showed evidence of contact loosening under these tests; this effect was traced to lack of proper contact adhesion in some stage of cell processing. As our contacting techniques have improved, the incidence of peeling has lessened considerably. The problem, at least in part, was a result of the way cell fabrication had to be carried out in the laboratory. Often cells had to wait, after LPE growth, for periods of days before the contacting operation could begin. This delay caused either a slight oxidation or contamination of the surface. It is extremely difficult to clean the surface of (AlGa) As because of its high reactivity, especially when extremely thin window layers are involved. When the cells are processed without undue delay or when sufficient precaution is taken to minimize oxidation, routine sputter-cleaning prior to contacting suffices to resolve the adhesion problem, as the marked improvement seen in our latest cells clearly demonstrates. The addition of some fluxing metal such as Cr or Ti prior to Au-Zn contacting may be another way of improving the surface cleaning of the cell. It is noteworthly that the silicon solar cell contacts were developed using a similar procedure.

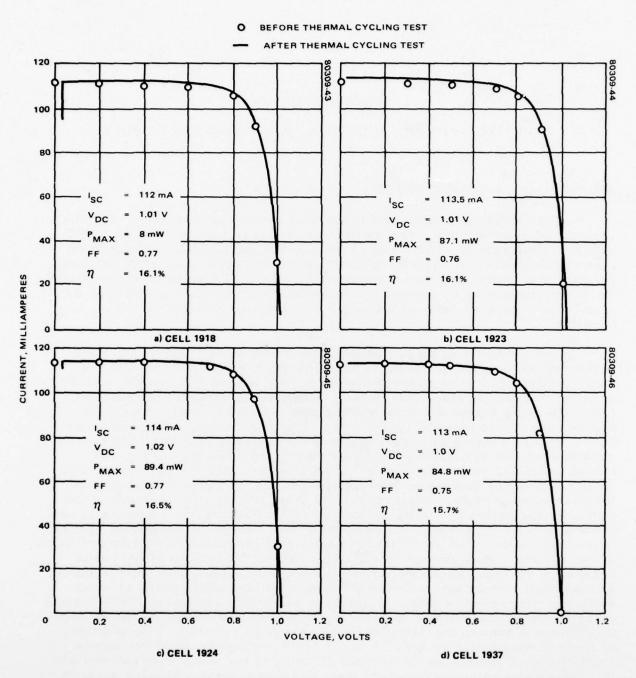


FIGURE 49. PHOTO I-V CHARACTERISTICS BEFORE AND AFTER THERMAL CYCLING TEST

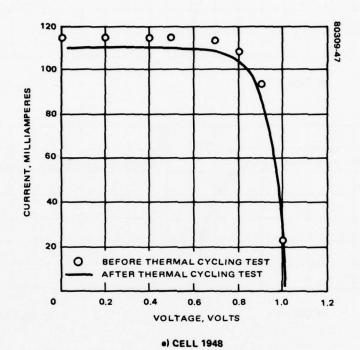


FIGURE 49.(CONTINUED). PHOTO I-V CHARACTERISTICS BEFORE AND AFTER THERMAL CYCLING TEST

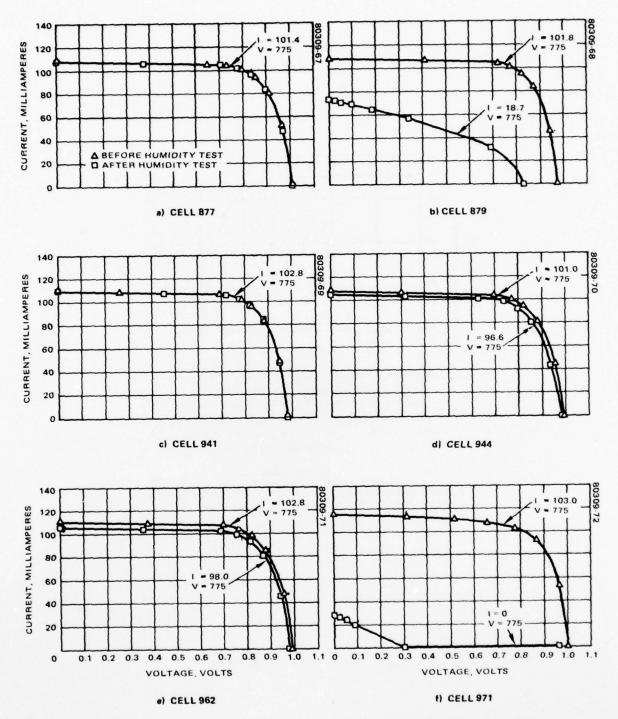


FIGURE 50. PHOTO I-V CHARACTERISTICS BEFORE AND AFTER HUMIDITY TEST

### 2. HUMIDITY TEST

Six cells with cover glasses were tested at a minimum temperature of 45°C and a relative humidity of at least 90 percent for a period of 10 days. As shown in Table 18, four of the cells exhibited negligible power degradation. Only two degraded significantly due to an opaque, white growth under the cover glass which initiated at the edge and progressed over the upper cell surface. The cause was traced to a processing step. Both these cells had been etched using hydrofluoric acid solution as a cleaning step. Apparently, a subsequent cleaning using deionized water was inadequate and left some absorbed fluoride ions on the surface that were activated during the humidity cycling. Such behavior has been observed in silicon cells as well.

For completeness, electrical characteristics of all six cells are shown in Figure 50. In addition, significant parameters are presented in Table 18. In the latter, before (B) and after (A) values of  $V_{\rm OC}$ , power at a specific voltage (775 mV) and  $I_{\rm SC}$  are compared. In addition, percentages of degradation are tabulated. Finally, two sets of average figures, with and without values for the two failed cells, are calculated. Significantly, if the two degraded cells can be ignored (since failure was not due to an inherent materials limitation of the cell), average degradation of the remaining cells fell well within acceptable levels.

## 3. TAPE PEEL TESTS

The tape peel tests we conducted confirm the argument of the preceding paragraph. Under the best conditions, when oxide formation was minimized and cell processing was expeditious, contacts to both n and p sides of the cell proved to be mechanically strong. However, when there were areas on the surface of the cell that were not clean and free of oxide, the tape peel test resulted in contact pull-off. Both visual contact appearance and peel test results improved considerably during the course of testing. It was found that this was directly related to increased sealing of the annealing furnace.

TABLE 18. ELECTRICAL PARAMETERS BEFORE AND AFTER HUMIDITY TEST

Cell ID	W <sub>OC</sub> , mV (B)	W <sub>OC</sub> , mV (A)	ΔV <sub>oc</sub> ,	P <sub>v=775</sub> , mW (B)	Pv=775, mW (A)	ΔP <sub>V=775</sub> .	mA (B)	Isc. mA (A)	ΔI <sub>SC</sub> .
944	1000.0	990.4	-0.96	78.28	74.87	-4.36	108.0	105.9	-1.94
879	980.8	838.4	-14.52	78.90	14.49	-81.63	108.0	74.0	-31.48
962	995.2	987.2	-0.80	79.67	75.95	4.66	110.4	105.9	-4.08
971	1009.6	979.2	-3.01	79.83	0	100.00	115.0	29.1	-74.70
877	1004.8	1003.2	-0.16	78.59	78.59	0	107.2	107.8	+0.56
941	974.4	982.4	+0.82	79.67	79.67	0	108.8	109.0	+0.18
Average 1	994.1	963.5	-3.08	79.16	53.93	-31.87	109.6	88.6	-19.16
Average 2°	993.6	990.8	-0.28	79.05	77.27	-2.25	108.6	107.2	-1.29

\*Average 2 disregards cells 879 and 971.

Note: Accuracy of values using the simulator is ±1.0%.

The Au-Ge-Ni-Ag n-type contact has been successfully used for soldering as well as to mount on metallic blocks (generally Mo). The integrity of these contacts is therefore deemed acceptable. The p-type contact (AuZn-Ag), however, remains imperfect. A weak adhesion is observed in random spots on the (AlGa)As. In many instances these spots can be traced to surface defects arising either from oxidation, as noted above, or from contamination. In other cases they can be traced to fine submicron gallium particles left on the surface when the layer is pulled out of the growth system. When these are removed by mechanical abrasion, they seem to leave a tail on the surface, and wherever tailing occurs, contact problems result. Some of the oxide problems are apparently caused by such tailing. We have developed cleaning methods that minimize tailing, and in our latest cells the improvement in adhesion between the contact and the surface has been remarkable.

As a result of these studies, we believe that the contacts can be made sufficiently strong to pass the tape peel test. However, in the laboratory environment it will be difficult to establish the operating conditions necessary to ensure complete reproducibility for cell contacts until the volume of cells warrants the setting up of a fabrication facility to handle the cells on a small pilot line basis.

### SECTION VIII

### WELDING STUDIES

GaAs cells fabricated at HRL were sent to the Space and Communications Group for attaching permanent interconnects to both the top and bottom metallized contacts using SCG's recently developed ultrasonic seam welder. Five such completed cells, with tabs of the maximum mechanical pull strength possible using optimum present technology, were to be processed. Optimum present technology involves not only the capability of the seam welding machine but also the latest contact metallizations of the cell, as well as cleaning and handling techniques. To accomplish such fabrication economically, extensive preliminary research was directed toward, first, Si and then to GaAs practice cells.

### 1. REQUIREMENT

GaAs cells fabricated at the Malibu facility were sent to the SCG Solar Panel Laboratory for the bonding of permanent leads or tabs to both the top and bottom metallized contacts using the ultrasonic seam welder apparatus.

The facility in producing repeatable, reliable welds is not constant but instead depends heavily on the particular conditions of the system to be welded. For example, the ability to weld thick Mo to polished sapphire will differ considerably from bonding Au leaf to severely abraded graphite. Thus, weldability is a function of, among aother things, substrate material, component surface conditions, contact/tab composition, and cross-sectional geometry, in addition to sensitive equipment controls and operation techniques. Because of this, a brief review of cell characteristics, tab characteristics, welding apparatus, and bonding procedure is in order.

## 2. CELL CHARACTERISTICS

The solar cells to be bonded were 2 x 2 cm x 14 mil devices formed by growing two GaAs epilayers onto an  $n^+$  bulk substrate doped to 1 x  $18^{18}$  cm<sup>-3</sup>. The first of these layers was n-type (1 x  $10^{17}$  cm<sup>-3</sup>) and between 15 to 20 microns in depth. The topmost epilayer was p-type

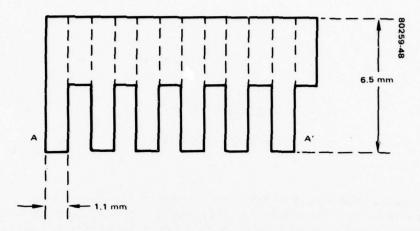


FIGURE 51. SILVER FOIL PATTERN CONSISTING OF SIX TABS

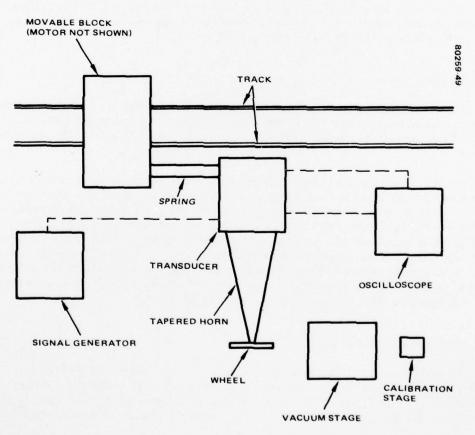


FIGURE 52. TOP VIEW SCHEMATIC OF ULTRASONIC WHEEL-WELDER AND SUPPORTING EQUIPMENT

(AlGa)As (1 x 10  $^{18}$  cm  $^{-3}$ ) and only 0.1 to 1.0 micron. Onto this latter surface was deposited an upper multimetal contact and grid pattern consisting of 250 Å of sputtered Zn-Au alloy superimposed with 5.0 $\mu$  (±2.0 $\mu$ ) of evaporated Ag. The grid pattern consisted of 24 evenly spaced lines tapering from 3.00 to 0.75 mil, all of which were joined to a 2 cm by 28 mil bus bar which in all cases was approximately 33 percent obstructed along its length by the 12 mil cover glass attached at a later stage of fabrication. The lower contact was formed over the entire bulk substrate by a 2000 Å deposition of simultaneously evaporated Au-Ge-Ni followed by 5.0 $\mu$  (±2.0 $\mu$ ) of evaporated Ag.

# 3. TAB CHARACTERISTICS

Tabs were constructed from 99.99 percent Ag foil 1.0 mil thick. Units prepared for welding were made up of six tabs, each originally connected as shown in Figure 51. Welds were made by placing the fingers over the solar cell contact and running the wheel from A to A'. The foil was then cut along the dashed lines and individually separated following the welding operation. Thus, attached to the completed cell were 12 independent tabs each approximately  $1.1 \times 6.5 \text{ mm}^2$  in area.

### 4. WELDING APPARATUS

A simplified block schematic of the ultrasonic seam welder and supporting equipment is shown in Figure 52 (the horizontal plane is the surface of the figure; the vertical direction is into the diagram). Here the welding tool is 0.71 inch diameter wheel machined from drill rod and attached to a 6 inch long tapered horn rigidly connected to a magnetostrictive (ferromagnetic) transducer. This entire unit is spring mounted to a block in such a way that the spring tension and thereby the contact force  $F_{\rm C}$  of the wheel against the device can be increased or decreased in the vertical direction by means of set screws (not shown). The block, in turn, can be motor driven along a track in the horizontal plane at various speeds.

The transducer is controlled by a UTI Power Logicon (Model 40C) equipped with both power and tuning adjustments. Relative scales associated with each ensures reproducibility of settings. Tuning is further facilitated using an HP oscilloscope (Model 122AR) displaying a Lissajous pattern resulting from simultaneously monitoring the current and voltage through the transducer.

The vacuum stage supports both the solar cell and tabs during welding while the calibration stage is used to determine the contact force  $F_{\text{C}}$  of the wheel by means of a simple switch circuit.

## 5. BONDING PROCEDURE

## Preliminary Operations

The first step toward producing repeatably reliable bonds entails preliminary trial and error test operations involving sensitive adjustment of equipment and techniques in order to determine the proper settings for the particular substrate/contact/tab system to be welded. At this stage a minimum of four parameters are of significance. Notably, all address themselves to the amount and mode of energy delivery to the interface between the tab and the contact surface of the cell:

- 1)  $F_c$ , contact force This force is that which the weld wheel exerts upon the tab/cell combination during welding. In the past it was determined by positioning the wheel upon the calibration stage which closed a circuit so that an indicator light was illuminated. A wire was looped around the horn and attached to a pull gauge and the wheel was lifted the minimal amount required to effect open circuit. A more direct method involved a two-handed procedure in which the wheel was repositioned upon the vacuum stage and a piece of paper was inserted in between. The wheel was then gauge lifted with one hand until the paper could be barely slipped away with the other. In either case  $F_c$  was capable of being adjusted through a range from zero to well over 450 grams.
- 2) P, relative power output of the UTI source This instrument converts 60 Hz to 60,000 Hz which, in turn, is introduced to the coil around the ferromagnetic core the heart of the transducer. This core is magnetostrictive: its physical dimensions (length) vary in response to the changes in the surrounding magnetic field. Thus, the 60,000 Hz electromagnetic waves are converted to 60,000 Hz mechanical oscillations forcing the wheel to vibrate horizontally. Thus, an adjustment in the amplitude of the electromagnetic wave translates into a change in energy delivered to the weld. Power is repeatable due to the unitless scale provided on the source.
- 3) T, tuning of the UTI source A 60,000 Hz mechanical wave travels down the 6 inch horn and is delivered to the wheel and, ultimately, the weld. For maximum energy level and minimum feedback vibrations the amplitude of the mechanical wave must be at its maximum at the tab-contact interface. If it is not, the wheel will be oscillating partly in response to the inducing 60,000 Hz magnetic signal and partly in response to reflected mechanical vibrations, causing a destructive (feedback) electrical impedance in the coil indicated by a phase shift in its current and voltage. Tuning alters slightly the frequency of the electrical signal and thereby the mechanical oscillations. This maximizes energy delivery to the wheel by matching the resonant frequency of the horn/wheel assembly. It is measured in relative, unitless values by a meter directly monitoring coil impedance.
- 4) V, velocity of the wheel during the welding operation Obviously, the longer the wheel rests on any given area of the weld, the more energy delivered to that area. If too great a velocity is used, then the energy imparted is too little to cause proper deformation and adhesion; too slow a

velocity, and the wheel abrades through the metals and even the cell itself. Velocity is adjusted reproducibly using, again, a relative but scaled control.

# Determination of Fc

An immediate concern was lack of adequate control of  $F_c$ . Neither of the two former methods of determining this setting was acceptable since resulting values often differed by over 100 grams. Significantly, measurements from neither were found to repeatably and accurately pinpoint the true force of the real case situation. Therefore, a simple indicator device was constructed similar to the one connected to the calibration stage but designed to measure the force of the wheel on the actual solar cell mounted on the vacuum stage itself. By means of this technique, the contact force was easily repeatable to within  $\pm 10$  grams.

#### 6. TAB PULL TESTS

After welding, tabs were separated and individually tested using the Unitek Micropull Tester (Model 6-092-03). Cells and each of their tabs were indexed for future reference and saved for possible further experimentation. In addition to an identification number and the pull force (in pounds), the weld condition and that of the metal area beneath the weld (after pulling) were tabulated for each cell. An explanation of the codes adopted and their significance is as follows:

### 1) Weld condition

- a) AO Already off. The weld was a total failure in that the tab did not adhere and was not available for pulling. AO always implies a pull force of zero.
- b) TO Tab off. During testing, the entire tab (the parts on both sides of the weld area) became totally dislodged. TO indicates a successful weld only for pulls ≥ 0.56 pound. For strengths less than this, TO implies:
  - (1) Weld failure if the metal under the weld area is completely intact (OK).
  - (2) Metal failure if the metal under the weld area is less than completely intact (NG).
- c) BAW Broke at weld. During testing the tab broke at the weld so that the pulled section was removed while the other portion remained. BAW indicates a successful weld only for pulls ≥ 0.56 pound. For strengths less than this, BAW implies a

weld failure, most likely due to excessive wheel force causing extraordinary deformation of the metals.

d) TB- Tab broke. During testing the tab itself broke. This may happen either because the weld was excessively strong or there was a defect in the tab before pulling. Therefore, by means of the associated pull force, TB can indicate an exceptionally good weld. On the other hand it can never imply anything negative about the weld or metal conditions.

### 2) Metal condition

- a) OK- After testing there was no visual evidence of any damage to the contact metallization of the cell. Thus, all metal layers are intact and nothing was removed by means of adhesion to the tab. Observation OK in the metal column does not in itself indicate an acceptable weld if pull force is ≤ 0.56 pound.
- b) NG After testing there was visual evidence that part or all of the metal contact was removed by the tab. Even though NG records metal damage, pull force may still indicate an acceptable weld if ≥ 0.56 pound.

### 7. STUDY RESULTS

## Silicon Cells

Using the method described above to measure  $F_c$ , the following optimum values were determined for silicon cells:

 $F_c = 200 \text{ grams}$ 

P = 6.0

V = 35

T = 0.80

AD-A066 616

HUGHES AIRCRAFT CO LOS ANGELES CALIF SPACE AND COMMU--ETC F/G 10/2 HIGH EFFICIENCY GAAS SOLAR CELL DEVELOPMENT.(U)
JAN 79 S KAMATH, G WOLFF F33615-76-C-2121

F33615-76-C-2121 NL

UNCLASSIFIED

2 of 2 AD A066616





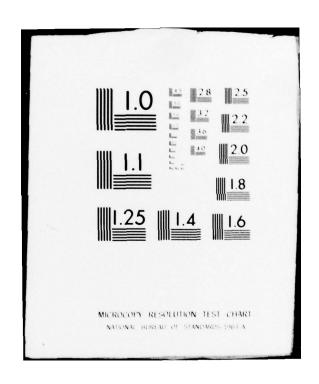












However, regardless of whether these or other settings were chosen, welding was less than reliable in the sense that with the same cell some tabs far exceeded minimum requirements (≥0.56 pound) while others failed. Table 19 presents typical results in which pull strengths ranged from 0.40 to 0.90 pound. Such a spread can be taken to indicate localized differences in the solar cell contact metallization. Significantly, with all silicon cells, all failures involved the welds themselves. In no case was there a loss of integrity in the device's metallization under and around the weld areas.

## GaAs Cells

On the basis of the results obtained for silicon cells, a number of GaAs cells were subjected to welding studies to determine optimum welding conditions. The parameters finally chosen were the following:

$$F_c = 260 \, \text{grams}$$

P = 8.0

V = 35

T = 0.49

TABLE 19. TAB PULL RESULTS FOR SILICON SOLAR CELL S101

			F <sub>c</sub> P V	= 6 = 3	00 gm 0 5 .80		
	Fre	ont Contact			- 1	Back Contact	
Tab No.	Pull Force, Ib	Weld Condition	Metal Condition	Tab No.	and the second second	Weld Condition	Metal Condition
1	0.90	ТВ	ок	1	0.75	BAW	ок
2	0.70	то	ок	2	0.60	то	OK
3	0.40	то	ок	3	0.25	то	ок
4	0.50	то	ок	4	0.25	то	ок
5	0.95	то	ок	5	0.25	то	OK
6	0.40	то	ок	6	0.10	то	ок

Tables 20 through 23 show the tab pull results for the GaAs solar cells tested. In general, it can be seen that welds to the front contacts were relatively successful. For the most part pull strengths exceeded 0.56 pound, regardless of the subsequent metal condition. On the other hand, back contact strengths were less consistently good, but low pull strengths were often attributed to poor adhesion of the metallization to the GaAs substrate rather than to inherent failure of the weld itself. However, in later cells, the adhesion of the back cells improved significantly. As a result, it is believed that with proper controls, ultrasonic welds can be successfully accomplished to GaAs cells with silver metallization.

TABLE 20. TAB PULL RESULTS FOR GaAs SOLAR CELL 2M928

			F <sub>C</sub> = P = V = T =	260 gm 8.0 35 0.49			
	Fre	ont Contact			В	ack Contact	
Tab No.	Pull Force, Ib	Weld Condition	Metal Condition	Tab No.	Pull Force, Ib	Weld Condition	Metal Condition
1	0.90	то	ок	1	0.50	то	NG
2	0.80	BAW	ок	2	0	AO	ОК
3	0.90	BAW	ок	3	0.30	BAW	ОК
4	0.20	то	ок	4	0.35	то	NG
5	0.80	то	ок	5	0.40	BAW	ок
6	0.95	то	ок	6	0.40	BAW	NG

TABLE 21. TAB PULL RESULTS FOR GaAs SOLAR CELL 2M1098

Fc	=	260 gm
P	=	8.0
V	=	35
Т	=	0.49

	Fre	ont Contact		Back Contact				
Tab No.	Pull Force, Ib	Weld Condition	Metal Condition	Tab No.	Pull Force, Ib	Weld Condition	Metal Condition	
1	0.85	то	NG	1	1.00	то	ок	
2	0	AO	NG	2	0.95	BAW	OK	
3	0.90	то	NG	3	0.80	BAW	OK	
4	0.85	то	NG	4	1.05	BAW	ок	
5	0.50	то	NG	5	0	AO	ок	
6	0.60	то	NG	6	0.35	то	ОК	

TABLE 22. TAB PULL RESULTS FOR GaAs SOLAR CELL 1E981

			Fc	=	290 gm			
			P	=	8.0			
			V	=	35			
			т	=	0.45			
	Fr	ont Contact				6	ack Contact	
Tab No.	Pull Force, Ib	Weld Condition	Metal Condition	on	Tab No.	Pull Force, Ib	Weld Condition	Metal Condition
1	0.68	TO/BAW	ОК		1	0	то	NG
2	1.01	то	OK		2	0.24	то	NG
3	1.11	то	NG		3	0.01	то	NG
4	0.64	то	NG		4	0.02	то	NG
5	0.64	TO/BAW	OK		5	0	то	NG
6	0.13	то	NG		6	0.51	то	NG

TABLE 23. TAB PULL RESULTS FOR GaAs CELL 1E1021A

F<sub>C</sub> = 290 gm
P = 8.0
V = 35
T = 0.45

Front Contact

	Front Contact				Pack Contact				
Tab No.	Pull Force, Ib	Weld Condition	Metal Condition	Tab No.	Pull Force, Ib	Weld Condition	Metal Condition		
1	0.60	TO/BAW	NG	1	•	•	•		
2	0.94	BAW	ОК	2					
3	1.00	ТВ	ОК	3					
4	0.91	BAW	NG	4					
5	0.86	BAW	ОК	5					
6	0.86	BAW	ОК	6					

<sup>\*</sup>Back contact not tested.

#### SECTION IX

### CONCLUSIONS

The study demonstrated the feasibility of fabricating GaAs cells using the Hughes infinite melt technique. Cells thus fabricated exhibit marked reproducibility in short circuit current and open circuit voltage. Midway through the program, 17.5 percent efficiency at AMO was achieved for the cells. With reduction in funding and the attendant necessity of reevaluating program goals, the decision was made to concentrate on increasing radiation resistance and cell performance reproducibility. In subsequent work, AMO efficiencies in the 17 percent range were again achieved, and improvements were made in contact integrity, cell reproducibility, and process control. Open circuit voltages are consistently above I volt, and short circuit currents are above 110 mA.

Further work is now required on packaging techniques, the next step in this direction being fabrication of GaAs cells on a pilot line basis in preparation for their large scale production. Results have established the advantages of the GaAs cell over silicon and its reproducibility in fabrication.

### REFERENCES

- 1. I.N. Shklyarevskii et al., Optics and Spec., Vol. 32, 1972, p. 406.
- 2. P. Stehle, J. Opt. Soc. Am., Vol. 53, 1963, p. 1003.
- 3. American Institute of Physics Handbook, 3rd edition, pp. 6-28, 6-29.
- 4. J. C. Burgiel et al., J. Electrochem. Soc., Vol. 115, 1968, p. 729.
- 5. W.M. Graven, J. Chem. Phys., Vol. 35, 1961, p. 1526.
- 6. Dow Corning data sheet XR-63-488.
- 7. R.C. Eden, Technical Report No. 5221-1 prepared under U.S. Army Contract DA44-009 AMC-1474(T) and Center for Material Research Contract SD-87.
- 8. G.S. Kamath et al., <u>Integrated Optics</u>, Final report AFCRL-TR-74-0542, October 1974, p. 27.
- H. J. Hovel and J. M. Woodall, <u>J. Electrochem. Soc.</u>, Vol. 120, 1973, p. 1249.
- 10. S.A. Abagyan and V.K. Sabashiev, Sov. Phys. Solid State, Vol. 6, 1965, p. 2529.
- 11. Anon, NASA SP8005, Revised May 1971.
- 12. C.T. Sah, R.N. Noyce, and W. Shockley, Proc. IRE, Vol. 45, September 1957, p. 1228.
- 13. H.J. Hovel, Proc. IEEE 10th Photovoltaic Specialists Conference, 1973, p. 34.
- J. M. Woodall and H. J. Hovel, App. Phys. Lett., Vol. 30, 1977, p. 492



- 15. G.S. Kamath, J. Ewan, and R.C. Knechtli, IEEG Trans. Elec. Dev., Vol. 24, 1977, p. 473.
- 16. J. Ewan, G.S. Kamath, R.C. Knechtli, Proc. 11th IEEE Photovoltaic Specialists Conf., 1975, p. 409.
- 17. G.S. Kamath, <u>Topical Mtg. on Integrated Optics Digest of Tech.</u>
  Papers, (New Orleans, LA), 1974.
- 18. R.I. Moon, et al., "Performance of (AlGa)As-GaAs Solar Cells in the Space Environment, "Proc. 12th IEEE Photovoltaic Specialists Conf., 1975, p. 255.
- 19. R.S. Miller and J.S. Harris, "Gallium Arsenide Concentration System" presented at AIAA Conference on the Future of Aerospace Power System, March 1977.
- 20. G.H. Walker and E.J. Conway, "Annealing of GaAs Solar Cells Damaged by Electron Irradiation," J. Electrochem. Soc., Vol. 125, No. 4, 1978, p. 676.

